1-1-2015

From Forced Collapse To H Ii Region Expansion In Mon R2: Envelope Density Structure And Age Determination With Herschel

P. Didelon

F. Motte

P. Tremblin

L. D. Anderson

Astronomy
&
Astrophysics

From forced collapse to H II region expansion in Mon R2: Envelope density structure and age determination with *Herschel*[⋆,⋆⋆]

P. Didelon[1], F. Motte[1], P. Tremblin[1,2,3], T. Hill[1,4], S. Hony[1,5], M. Hennemann[1], P. Hennebelle[1], L. D. Anderson[6,7],
F. Galliano[1], N. Schneider[1,8], T. Rayner[9], K. Rygl[10], F. Louvet[1,11], A. Zavagno[12], V. Könyves[1], M. Sauvage[1],
Ph. André[1], S. Bontemps[8], N. Peretto[1,9], M. Griffin[9,13], M. González[1], V. Lebouteiller[1], D. Arzoumanian[1],
J.-P. Bernard[14], M. Benedettini[15], J. Di Francesco[16,17], A. Men'shchikov[1], V . Minier[1], Q. Nguyễn Lương[1,18],
P. Palmeirim[1], S. Pezzuto[15], A. Rivera-Ingraham[19], D. Russeil[12], D. Ward-Thompson[8,20], and G. J. White[21,22]

(Affiliations can be found after the references)

Received 1 April 2015 / Accepted 13 July 2015

ABSTRACT

Context. The surroundings of H II regions can have a profound influence on their development, morphology, and evolution. This paper explores the effect of the environment on H II regions in the MonR2 molecular cloud.

Aims. We aim to investigate the density structure of envelopes surrounding H II regions and to determine their collapse and ionisation expansion ages. The Mon R2 molecular cloud is an ideal target since it hosts an H II region association, which has been imaged by the *Herschel* PACS and SPIRE cameras as part of the HOBYS key programme.

Methods. Column density and temperature images derived from *Herschel* data were used together to model the structure of H II bubbles and their surrounding envelopes. The resulting observational constraints were used to follow the development of the Mon R2 ionised regions with analytical calculations and numerical simulations.

Results. The four hot bubbles associated with H II regions are surrounded by dense, cold, and neutral gas envelopes, which are partly embedded in filaments. The envelope's radial density profiles are reminiscent of those of low-mass protostellar envelopes. The inner parts of envelopes of all four H II regions could be free-falling because they display shallow density profiles: $\rho(r) \propto r^{-q}$ with $q \leqslant 1.5$. As for their outer parts, the two compact H II regions show a $\rho(r) \propto r^{-2}$ profile, which is typical of the equilibrium structure of a singular isothermal sphere. In contrast, the central UCH II region shows a steeper outer profile, $\rho(r) \propto r^{-2.5}$, that could be interpreted as material being forced to collapse, where an external agent overwhelms the internal pressure support.

Conclusions. The size of the heated bubbles, the spectral type of the irradiating stars, and the mean initial neutral gas density are used to estimate the ionisation expansion time, $t_{exp} \sim 0.1$ Myr, for the dense UCH II and compact H II regions and ~0.35 Myr for the extended H II region. Numerical simulations with and without gravity show that the so-called lifetime problem of H II regions is an artefact of theories that do not take their surrounding neutral envelopes with slowly decreasing density profiles into account. The envelope transition radii between the shallow and steeper density profiles are used to estimate the time elapsed since the formation of the first protostellar embryo, $t_{inf} \sim 1$ Myr, for the ultra-compact, 1.5−3 Myr for the compact, and greater than ~6 Myr for the extended H II regions. These results suggest that the time needed to form a OB-star embryo and to start ionising the cloud, plus the quenching time due to the large gravitational potential amplified by further in-falling material, dominates the ionisation expansion time by a large factor. Accurate determination of the quenching time of H II regions would require additional small-scale observationnal constraints and numerical simulations including 3D geometry effects.

Key words. ISM: individual objects: Mon R2 – stars: protostars – ISM: structure – dust, extinction – H II regions

1. Introduction

Molecular cloud complexes forming high-mass stars are heated and structured by newly born massive stars and nearby OB clusters. This is especially noticeable in recent *Herschel* observations obtained as part of the HOBYS key programme, which is dedicated to high-mass star formation (Motte et al. 2010, 2012)[1]. The high-resolution (from 6″ to 36″), high-sensitivity observations obtained by *Herschel* provide, through spectral energy distribution (SED) fitting, access to temperature and column density maps covering entire molecular cloud complexes. It has allowed us to make a detailed and quantitative link between the spatial and thermal structure of molecular clouds for the first time. Heating effects of OB-type star clusters are now clearly observed to develop over tens of parsecs and up to the high densities (i.e. ~10^5 cm^{-3}) of starless cores (Schneider et al. 2010b; Hill et al. 2012; Roccatagliata et al. 2013). Long known at low- to intermediate-densities, it has recently been reported that cloud compression and shaping lead to the creation of very high-density filaments hosting massive dense cores ($10^5–10^6$ cm^{-3}, Minier et al. 2013; Tremblin et al. 2013). While triggered star formation is obvious around isolated H II regions (Zavagno et al. 2010; Anderson et al. 2012; Deharveng et al. 2012), it has not yet been unambiguously established as operating across whole cloud complexes (see Schneider et al. 2010b; Hill et al. 2012).

The Mon R2 complex hosts a group of B-type stars, three of them associated with a reflection nebula (van den Bergh 1966). Located 830 pc from the Sun, it spreads over 2 deg (~30 pc at this distance) along an east-west axis and has an age of ~1−6×10^6 yr (Herbst & Racine 1976, see Plate V). This reflection nebulae association corresponds to the Mon R2 spur seen in CO (Wilson et al. 2005). An infrared cluster with a similar age (~1−3×10^6 yr, Aspin & Walther 1990; Carpenter et al. 1997) covers the full molecular complex and its H II region association area (Fig. 1 in Gutermuth et al. 2011). The western part of the association hosts the most prominent object in most tracers. This UCH II region (Fuente et al. 2010), which is powered by a B0-type star (Downes et al. 1975), is associated with the infrared source Mon R2 IRS1 (Massi et al. 1985; Henning et al. 1992). The UCH II region drives a large bipolar outflow (Richardson et al. 1988; Meyers-Rice & Lada 1991; Xie & Goldsmith 1994) that is oriented NW-SE and is approximately aligned with the rotation axis of the full cloud found by Loren (1977). The molecular cloud is part of a CO shell with ~26 pc size whose border encompasses the UCH II region (Wilson et al. 2005). The shell centre is situated close to VdB72/NGC 2182 (Xie & Goldsmith 1994; Wilson et al. 2005) at the border of the temperature and column density map area defined by the Herschel SPIRE and PACS common field of view (see e.g. Fig. F.1). Loren (1977) also observed CO motions that he interpreted as tracing the global collapse of the molecular cloud with an infall speed of a few km s^{-1}. This typical line profile of infall has also been seen locally in CO and marginally in ^{13}CO near the central UCH II region thanks to higher resolution observations (Tang et al. 2013). Younger objects, such as molecular clumps seen in CO, H$_2$CO, and HCN, for example, have been observed in this molecular cloud (e.g. Giannakopoulou et al. 1997).

In this paper, we constrain the evolutionary stages of the Mon R2 H II regions through their impact on the temperature and the evolution of the density structure of their surrounding neutral gas envelopes. The evolution and growth of the H II region as a function of age depends strongly on the density structure of the surrounding environment. If a simple expansion at the thermal sound speed determines their sizes, the number of UCH II regions observed in the galaxy exceeds expectations. This is the so-called lifetime problem (Wood & Churchwell 1989b; Churchwell 2002) that partly arises from a mean density and a mean ionising flux representative of a sample but perhaps not adapted to an individual object. To precisely assess the UCH II lifetime problem, we need an accurate measure of the observed density profile of the neutral envelope outside of the ionised gas.

One goal of this paper is to use the sensitive *Herschel* far-infrared (FIR) and sub-mm photometry of the compact H II regions in MonR2 to constrain these profiles and subsequently estimate the H II regions ages based on measured profiles and the corresponding average density. Moreover, *Herschel* measurements are sensitive enough that we can even investigate significant changes in the density profile with radial distance. Such changes may be signposts of dynamical processes, such as infall or external compression.

The paper is organised as follows. *Herschel* data, associated column density, dust temperature images, and additional data are presented in Sect. 2. Section 3 gives the basic properties of H II regions and the density structure of their surrounding envelopes. These constraints are used to estimate H II region expansion in Sect. 4 and the age of the protostellar accretion in Sect. 5, to finally get a complete view of the formation history of these B-type stars.
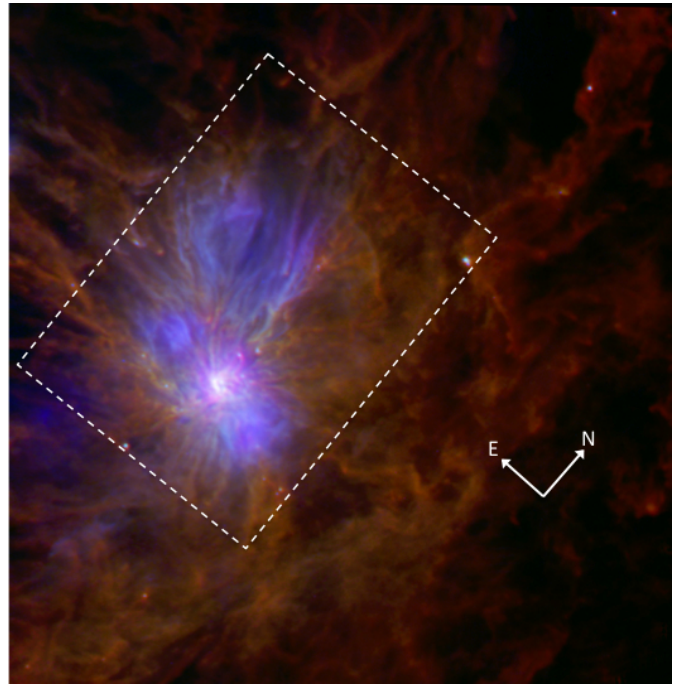
Fig. 1. Three-colour *Herschel* image of the Mon R2 molecular complex using 70 μm (blue), 160 μm (green), and 250 μm (red) maps. The shortest wavelength (blue) reveals the hot dust associated with H II regions and protostars. The longest wavelength (red) shows the cold, dense cloud structures, displaying a filament network. The dashed rectangle locates the four H II region area shown in Fig. 2.

2. Data

2.1. Observations and data reduction

Mon R2 was observed by *Herschel* (Pilbratt et al. 2010) on September 4, 2010 (OBSIDs: 1342204052/3), as part of the HOBYS key programme (Motte et al. 2010). The parallel-scan mode was used with the slow scan-speed (20″/s), allowing simultaneous observations with the PACS (70 and 160 μm; Poglitsch et al. 2010) and SPIRE (250, 350, 500 μm; Griffin et al. 2010) instruments at five bands. To diminish scanning artefacts, two nearly perpendicular coverages of 1.1°×1.1° were obtained. The data were reduced with version 8.0.2280 of HIPE[2] standard steps of the default pipeline up to level 1, including calibration and deglitching, and were applied to all data. The pipeline was applied (level-2) further, including destriping and map making, for SPIRE data. To produce level-2 PACS images, we used the *Scanamorphos* software package[3] v13, which performs baseline and drift removal before regriding (Roussel 2013). The resulting maps are shown in Rayner et al. (in prep.). The map angular resolutions are 6″−36″, which correspond to 0.025−0.15 pc at the distance of Mon R2.

The *Herschel* 3-colour image of the Mon R2 molecular complex shows that the central UCH II region, seen as a white spot in Fig. 1, dominates and irradiates its surroundings. Three other H II regions exhibit similar but less pronounced irradiating effects (see the bluish spots in Fig. 1). These H II regions develop into a clearly structured environment characterised by cloud filaments.

---

[2] HIPE is a joint development software by the Herschel Science Ground Segment Consortium, consisting of ESA, the NASA *Herschel* Science Center, and the HIFI, PACS, and SPIRE consortia.
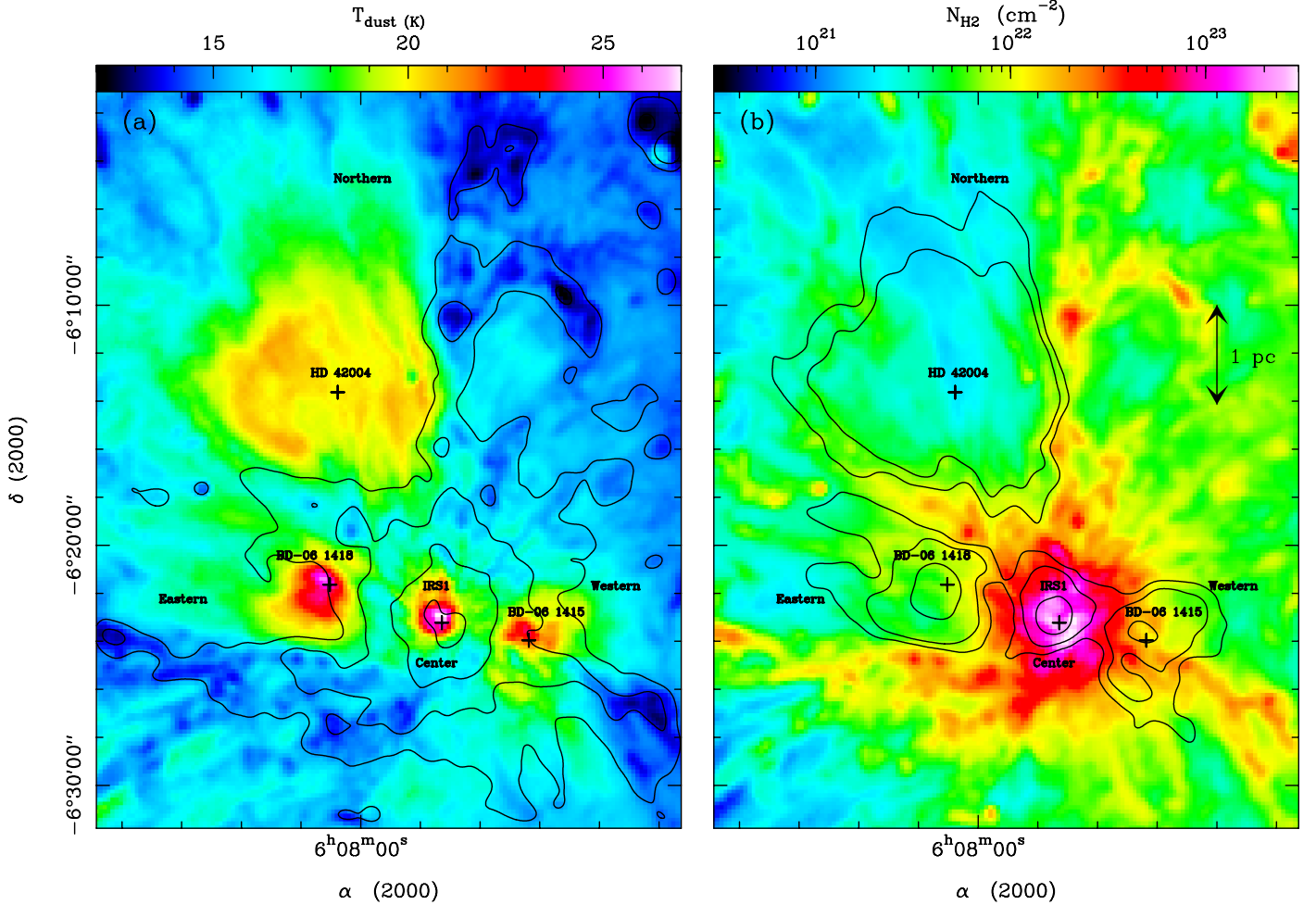
[3] http://www2.iap.fr/users/roussel/herschel/index.html

Fig. 2. Dust temperature (colours in **a**) and contours in **b**)) and column density (colours in **b**) and contours in **a**)) maps of the central part of the Mon R2 molecular cloud complex, covering the central, western, eastern, and northern H II regions with 36″ resolution. The heating sources of H II regions are indicated by a cross and with their name taken from Racine (1968) and Downes et al. (1975). Smoothed temperature and column density contours are 17.5, 18.5, and 21.5 K and 7×10^{21}, 1.5×10^{22}, 5×10^{22}, and 1.8×10^{23} cm^{-2}.

2.2. Column density and dust temperature maps

The column density and dust temperature maps of Mon R2 were drawn using pixel-by-pixel SED fitting to a modified blackbody function with a single dust temperature (Hill et al. 2009). We used a dust opacity law similar to that of Hildebrand (1983), assuming a dust spectral index of $\beta = 2$ and a gas-to-dust ratio of 100, so that dust opacity per unit mass column density is given by $\kappa_\nu = 0.1 \, (\nu/1000 \text{ GHz})^\beta$ cm^2 g^{-1}, as already used in most HOBYS studies (e.g. Motte et al. 2010; Nguyen-Luong et al. 2013). The 70 μm emission very likely traces small grains in hot PDRs and so was excluded from the fits because it does not trace the cold dust used to measure the gas column density (Hill et al. 2012).

We constructed both the four-band (T_{4B}) and three-band (T_{3B}) temperature images and associated column density maps by either using the four reddest bands (160 to 500 μm) or only the 160, 250, and 350 μm bands of *Herschel* (cf. Hill et al. 2011, 2012). Prior to fitting, the data were convolved to the 36″ or 25″ resolution of the 500 μm (resp. 350 μm) band and the zero offsets, obtained from comparison with Planck and IRAS (Bernard et al. 2010), were applied to the individual bands. The quality of a SED fit was assessed using χ^2 minimisation. Given the high quality of the *Herschel* data, a reliable fit can be done even when dropping the 500 μm data point. For most of the mapped points, which have medium column density and

average dust temperature values, N_{H2} and T_{dust} values are only decreased by 10% and increased 5%, respectively, between T_{4B} and T_{3B}. In the following, we used the column density or temperature maps built from the four longest *Herschel* wavelengths, except when explicitly stated. The high-resolution T_{3B}, $I_{70 \, \mu m}$, and $I_{160 \, \mu m}$ maps have only been used for size measurements, not for profile-slope determinations.

The resulting column density map shows that the central UCH II region has a structure that dominates the whole cloud with column densities up to $N_{H2} \sim 2 \times 10^{23}$ cm^{-2} (see Figs. 2b and F.1). In its immediate surroundings, i.e. $\sim$1 pc east and west, as well as $\sim$2.5 pc north, the temperature map of Fig. 2a shows two less dense H II regions and one extended H II region, respectively. The name and the spectral type of the stars that create these four H II regions are taken from Racine (1968) and Downes et al. (1975). Three are associated with reflection nebulae and are called IRS1, BD-06 1418 (vdB69), BD-06 1415 (vdB67), and HD 42004 (vdB68) (see Figs. 2a, b, F.2 and Table 1). The central UCH II region is located at the junction of three main filaments and a few fainter ones, giving the overall impression of a "connecting hub" (Fig. 2b). The three other H II regions are developing within this filament web and within the UCH II cloud envelope, which complicates study of their density structure.

The dust temperature image of Figs. 2a and F.2 shows that the mean temperature of the cloud is about 13.5 K and that

Table 1. Properties of the four H II region bubbles of Mon R2.

| Region name | Type | Exciting star from visual spectra | | | Ionisation from 21 cm free-free | | | $R_{\rm H\,II}$ | $\rho_{\rm e}$ |
| | | Ident. | Sp.T. | A_V[mag] | $S_{\rm 21cm}$ [mJy] | $N_{\rm Lyc}$ [s^{-1}] | Sp.T. | [pc] | [cm^{-3}] |
(1)	(2)	(3)	(4)	(5)	(6)	(7)	(8)	(9)	(10)
central	UC	IRS1	–	–	4114.	2.4×10^{47}	B0	0.09 ± 0.01	3200
western (vdB67)	Compact	BD-06 1415	B1	2.7	27.4	1.6×10^{45}	B1	0.11 ± 0.01	~200
eastern (vdB69)	Compact	BD-06 1418	B2.5	1.7	2.2	1.3×10^{44}	B2.5	0.08 ± 0.01	~100
northern (vdB68)	Extended	HD 42004	B1.5	1.6	38.	2.2×10^{45}	B1	0.8 ± 0.05	~10

Notes. The Mon R2 UCH II region is also called G213.71-12.6 or IRAS 06052-0622. Spectral types in Cols. 4 and 8 are given by Racine (1968) from visual spectra and from $N_{\rm Lyc}$ estimates derived from NVSS 21 cm data and Eq. (1) (see Cols. 6, 7). Extinctions given in Col. 5 are estimated from $E(B − V)$ given by Herbst & Racine (1976). The radii and electron density of the H II region bubbles (Cols. 9, 10) are estimated from the *Herschel* dust temperature and column density images (see Sects. 3.2−3.5).

it increases up to ~27 K within the three compact and ultra-compact H II regions. Dust temperature maps only trace the colder, very large grains and are not sensitive to hotter dust present within H II regions (see Anderson et al. 2012, Fig. 7). The temperature obtained from FIR *Herschel* SED corresponds to dust heated in the shell or PDR and thus directly relates to the size of the ionised bubble.

2.3. Radio fluxes and spectral type of exciting stars

We first estimated the spectral type of exciting stars from their radio fluxes. To do so, we looked for 21 cm radio continuum flux in the NVSS images (Condon et al. 1998), as well as in the corresponding catalogue[4]. The three compact H II regions delineated by colours and the temperature contours of Fig. 2 all harbour one single compact 21 cm source (see Table 1). The more developed northern H II region contains several 21 cm sources, whose cumulated flux can account for the total integrated emission of the region. We calculated the associated Lyman continuum photon emission, using the NVSS 21 cm flux listed in Table 1 and the formulae below, taken from Martín-Hernández et al. (2005), for example,

$$N_{\rm Lyc} = 7.6 \times 10^{46}\ {\rm s}^{-1} \times \left(\frac{S_\nu}{\rm Jy}\right)\left(\frac{T_{\rm e}}{10^4\ {\rm K}}\right)^{-\frac{1}{3}}\left(\frac{d}{\rm kpc}\right)^2 \times b(\nu, T_{\rm e})^{-1},\ (1)$$

where S_ν is the integrated flux density at the radio frequency ν, $T_{\rm e}$ is the electron temperature, d is the distance to the source, and the function $b(\nu, T_{\rm e})$ is defined by

$$b(\nu, T_{\rm e}) = 1 + 0.3195 \log\left(\frac{T_{\rm e}}{10^4\ {\rm K}}\right) - 0.213 \log\left(\frac{\nu}{\rm GHz}\right). \quad (2)$$

Quireza et al. (2006) determined an electron temperature of ~8600 K for the central UCH II region from radio recombination lines. We adopt the same temperature for the other H II regions since this $T_{\rm e}$ value is close to the mean value found for H II regions (see e.g. Quireza et al. 2006, Table 1). Using the $N_{\rm Lyc}$ estimates of Table 1 and the calibration proposed by Panagia (1973), we assumed that a single source excites the H II regions of Mon R2 and estimated their spectral type (see Table 1). These radio spectral types from B2.5 to B1 agree perfectly with those deduced from the visual spectra of Racine (1968[5]; see Table 1). We calculated $N_{\rm Lyc}$ for the Mon R2 UCH II region using six

other radio fluxes with wavelengths from 1 to 75 cm available in Vizier. They all have radio spectral types ranging from O9.5 to B0, which also agrees with previous estimates (Massi et al. 1985; Downes et al. 1975). The concordance of spectral types derived from flux at different radio wavelengths, including the shortest ones, confirm the free-free origin of the centimetre fluxes with a limited synchrotron contamination.

2.4. H II region type classification

Wood & Churchwell (1989b, end of Sects. 4.a and 4.c.xi) previously classified Mon R2 as an UCH II region. Considering the sizes and densities determined in Sect. 3.2, we define the morphological type of the four H II regions. The values from the central H II region ($\rho_{\rm e} = 3.2 \times 10^3\,{\rm cm}^{-3}$, $R_{\rm H\,II} = 0.09$ pc) are compatible with the range of oberved values for UCH II regions (e.g. Hindson et al. 2012), $\rho_{\rm e} = 0.34−1.03 \times 10^4\ {\rm cm}^{-3}$ and $R_{\rm H\,II} = 0.04−0.11$ pc. It agrees with the classification obtained from IRAS fluxes[6]. The western and eastern H II regions have similar small sizes (around 0.1 pc) but lower densities (<1000 cm^{-3}), which we assume to be more characteristic of compact H II regions. The northern H II region is larger (close to 1 pc) and has the very low density (<100 cm^{-3}) typical of extended H II regions.

3. Modelling of the H II regions' environment

The initial dense cloud structures inside which the high-mass protostars have been formed and the H II regions that have developed could have been considerably modified by both the protostellar collapse and the H II region ionisation. The bubble and shell created by the expansion of H II region retains information about its age and the mean density of the inner protostellar envelope whose gas has been ionised or collected. We hereafter investigate all of the components needed to describe the environment of H II regions. The density model is presented in Sect. 3.1. We first focus on the inner components that are directly associated with H II regions and which are generally studied at cm-wave radio, optical, or near-infrared wavelengths (see Sects. 3.2 and 3.3). We then characterise the component best studied by our *Herschel* data in detail, namely the surrounding cold neutral envelope (Sect. 3.4). We finally jointly use all available pieces of information to perform a complete density modelling in Sect. 3.5.

---

[4] NVSS : NRAO VLA Sky Survey, http://www.cv.nrao.edu/nvss/

[5] The spectral types from Herbst & Racine (1976) were not used because they misidentified vdB 68 and vdB 69 (see Loren 1977, note 1) and because Racine (1968) used better spectral resolution.

[6] The MonR2 IRAS fluxes donwloaded from Simbad ($F_{12} = 470$ Jy, $F_{25} = 4100$ Jy, $F_{60} = 13\,070$ Jy, and $F_{100} = 20\,200$ Jy) fulfil the Wood & Churchwell (1989a) and Kurtz et al. (1994) criteria: $\log(F_{25}/F_{12}) = 0.94 > 0.57$, $\log(F_{60}/F_{12}) = 1.44 > 1.3$, and $F_{100} > 1000$ Jy.

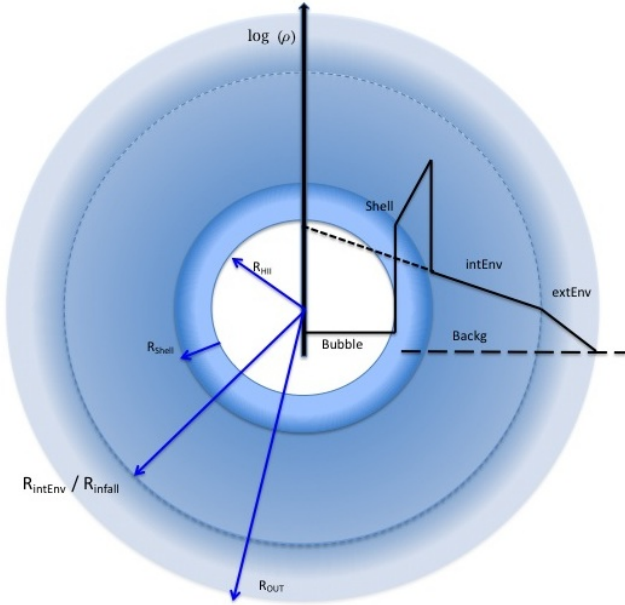### 3.1. Model of H II regions and their surroundings

Modelling of the observed column density and temperature structure of H II regions and their surroundings (Fig. 2) requires four density components (see Fig. 3): a central ionised bubble, a shell concentrating almost all of the collected molecular gas, a protostellar envelope decreasing in density, and a background. The background corresponds to the molecular cloud inside which the H II region is embedded. The three other components are proper characteristics of the H II region and its envelope. The envelopes of the three compact and UCH II regions are not correctly described by a single power law, but require two broken power laws similar to that of the inside-out collapse protostellar model (Shu 1977; Dalba & Stahler 2012; Gong & Ostriker 2013).

3.2. Extent of H II regions

H II region sizes are important for measuring because they constrain the age and evolution of the regions. Sizes are generally computed from Hα or radio continuum observations that directly trace the ionised gas. Such data are not always available. Potentially, Hα could be attenuated for the youngest H II regions, and radio continuum surveys frequently have relatively low resolution. We can instead use *Herschel* temperature maps, as well as $70\,\mu m$ and $160\,\mu m$ images to estimate the size of the H II regions.

The extent of all four H II regions can clearly be seen in the dust temperature map shown in Fig. 2a. This is an indirect measure since the *Herschel* map traces the temperature of big dust grains that dominate in dense gas and which reprocess the heating of photo-dissociation regions (PDRs) associated with H II regions. Such a dust temperature map provides the temperature averaged over the hot bubbles in the H II region and colder material seen along the same line of sight. This is particularly clear when inspecting the western H II region, which is powered
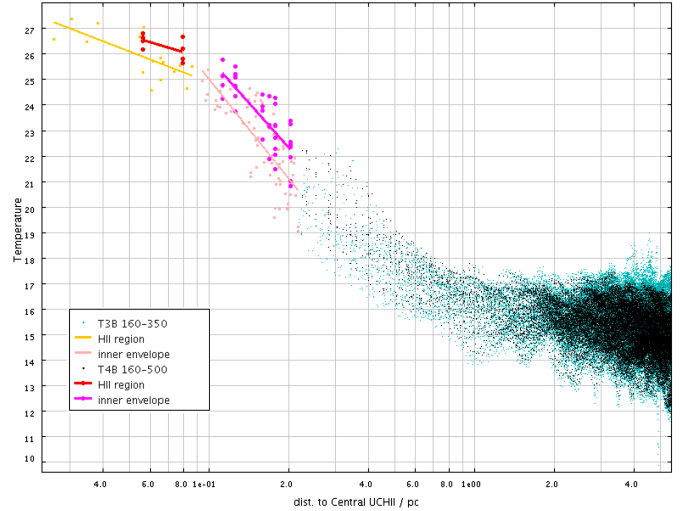

Fig. 4. Dust temperature radial profiles of the central UCH II region showing a steep outer part and a flatter inner region. We note the agreement of the measurements done with the 3-band temperature map, T_{3B} (red and magenta lines and points), and with the 4-band temperature map, T_{4B} (yellow and pink lines and points).

by BD-06 1415, since its temperature structure is diluted and distorted by the filament crossing its southern part. We used both the T_{4B} and T_{3B} temperature images with 36″ and 25″ resolutions. For the large northern extended H II region, the T_{4B} map alone would be sufficient since the angular resolution is not a problem. For the three other H II regions, we need to use the T_{3B} map, as well as $70\,\mu m$ and $160\,\mu m$ maps where intensities are used as temperature proxies (see discussion by Compiègne et al. 2011; Galliano et al. 2011). The 70 μm emission traces the hot dust and small grains in hot PDRs, which mark the borders of H II regions and thus define their spatial extent.

Despite the inhomogeneous and filamentary cloud environment of the Mon R2 H II regions, the heated bubbles have a relatively circular morphology (see Fig. 2a). This is probably due to the ionisation expansion, which easily blows away filaments and dense structures (e.g. Minier et al. 2013). To more precisely define the H II region sizes, we computed temperature radial profiles azimuthally averaged around the heating and ionising stars, which are shown in Figs. 2a, b. The resulting temperature profiles of the four H II regions share the same general shape: a slowly-decreasing central part surrounded by an envelope where the temperature follows a more steeply decreasing power law (see e.g. Fig. 4). We used the intersection of these two temperature structures to measure the radius of the flat inner part, which we use as an estimator of the H II region radius, R_{HII} (see Table 1). At the junction between the two temperature components, data scattering and deviation from a flat inner part leads to uncertainties of about 15%. The higher resolution T_{3B}, $70\,\mu m$, and $160\,\mu m$ maps confirm the derived R_{HII} values and reach a confidence level of ~10% uncertainty.

For the (small) central UCH II region, the radial profiles of the T_{3B} and T_{4B} temperatures are shown in Fig. 4. The flux profiles obtained from the $70\,\mu m$ and $160\,\mu m$ images with 6″ and 12″ resolutions are shown in Fig. 5. These four different estimators display similar radial shapes for the H II region and give consistent size values: $R_{HII} \simeq 0.09, 0.08, 0.09$, and 0.09 pc for $70\,\mu m$, $160\,\mu m$, T_{3B}, and T_{4B}, respectively. Similarly, concordant measurements are found for the fully resolved northern H II region in the T_{4B} and T_{3B} maps: $R_{HII} \simeq (0.85 \pm 0.05)$ pc. Interestingly, for the central UCH II region, the derived R_{HII}
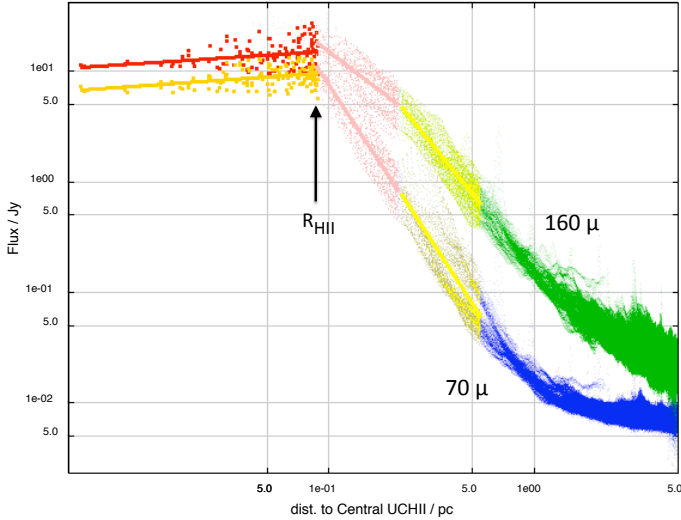
Fig. 5. Radial intensity profiles of the central UCH II region showing the measurements done at $70\,\mu m$ (blue points) and $160\,\mu m$ (green points) taking advantage of the PACS highest resolution, compared with the 3-band temperature (T_{3B}) and the 4-band temperature (T_{4B}) data given by the black arrow. The $160\,\mu m$ profile decreases less in the inner part of the envelope (pink line) than in its outer part (yellow line). Since $160\,\mu m$ emission is sensitive to dust temperature and density, this behaviour is probably related to the two different slopes found for the density profile of the envelope characterised in Sect. 3.4.1. The slope change indeed occurs at similar R_{Infall} radius.

value of ~0.09 pc is in excellent agreement with the one deduced from H42α RRL measurements (~0.08 pc, see Pilleri et al. 2012), showing that hot dust and ionised gas are spatially related. Radio continuum data and infrared [Ne II] line also give similar sizes and shapes (Massi et al. 1985; Jaffe et al. 2003).

Using Lyman flux (Table 1 Col. 7) and H II region size (Table 1 Col. 9) we use Eq. (5) to compute the corresponding electron density ρ_e, given in Col. 10.

3.3. H II region shells and their contribution to column density

Dense shells have been observed around evolved H II regions within simple and low-column density background environments (e.g. Deharveng et al. 2005; Churchwell et al. 2007; Anderson et al. 2012). The "collect-and-collapse" scenario proposes that the material ionised by UV flux of OB-type stars is indeed efficiently sweeping up some neutral gas originally located within the present H II region extent and developing a shell at the periphery of H II bubbles (Elmegreen & Lada 1977).

In Appendices D and E we investigate the contribution of this very narrow component to the column density measured with *Herschel*. Appendix D shows the beam dilution of the column density expected from the shell shoulder. Appendix E explores the density attenuation due to bubble and shell expansion in different types of envelope density profile. These two effects combined reduce the importance of the shell and predicts a decrease in the observed column density of H II regions with expansion at least in decreasing-density envelopes. The shell of the central UCH II region characterised by Pilleri et al. (2014, 2013) has an unnoticeable contribution to the high column density of the envelope. Even in the northern region, which is the most extended and favourable to the detection of a shell, the shell characteristics are uncertain due to the filamentary environment inside which the H II region developed (see Fig. 8). It shows that the shell is not a dominant component of the column density structure of the

H II regions studied here, but it cannot be neglected a priori from modelling.

3.4. The envelope surrounding H II regions

Amongst the crucial parameters influencing the expansion of an H II region and the size of the heated/ionised regions, we need to characterise the density profiles of their neutral envelopes. We therefore constructed radial column density profiles by plotting the N_{H_2} map around each of the ionising sources shown in Fig. 2b. Figures 6 shows the column density profiles of the central UCH II and eastern H II regions, respectively. The colours used for the different radial parts of the profiles are similar to those used for the temperature profiles of Fig. 4.

Radial column density profiles exhibit relatively flat inner parts that provide a reliable measurement of the column density maximum value, N_{H2}^{Max}, of the envelope surrounding each of the four H II regions (see Table 3, Col. 7). The sizes of these envelopes, given by the radius at half maximum, R_{HM}, were measured on the column density profile and range from 0.35 pc to 1.5 pc (see Table 3, Col. 8).

Assuming a spherical geometry that agrees with the shape of H II regions studied here, for which R_{HM} can be used as a size estimator, we can roughly estimate the observed mean density, $\langle \rho_{obs} \rangle$, from the maximum of the surface density N_{H2}^{Max}, using the equation

$$\langle \rho_{obs} \rangle \ = \ \frac{n}{V} = \frac{\pi \times R_{HM}^2 \, N_{H2}^{Max}}{\frac{4}{3} \pi \times R_{HM}^3} = \frac{3}{4} \times \frac{N_{H2}^{Max}}{R_{HM}}. \qquad (3)$$

This mean density corresponds to the presently observed state of the envelope (see Table 3, Col. 9). To estimate the initial mean density of the envelope, $\rho_{initial}$, before the ionisation starts, Sect. 3.5 suggests another way to determine it through its actual maximum density and density profile slope.

Comparison of the central UCH II region's characteristics shows good agreement, as deduced here with the parameters of the model used by Pilleri et al. (2012). The model has an envelope size of 0.34 pc, inner radius of 0.08 pc, and a mean density ~0.8×10^5 cm^{-3} comparable to our estimates: $R_{H II} \sim 0.09$ pc $R_{HM} \sim 0.35$ pc, $\langle \rho_{obs} \rangle = 1.4 \times 10^5$ cm^{-3}.

3.4.1. Column density profiles

With the model of Fig. 3 in mind, we characterise the four main components associated with H II regions and their surroundings in detail. The H II region bubble, fitted by a yellow line, corresponds to a temperature plateau and has an almost constant column density in Fig. 6. Surrounding the H II region, one can find the cloud envelope, which has a constantly decreasing temperature profile and splits here into slowly and sharply decreasing N_{H_2} parts, fitted by pink and blue lines in Fig. 6. As for the eastern H II region, the column density is lower and the inner envelope extent is larger, allowing a better distinction between the different envelope parts than in the central UCH II region. In this context, we define the inner envelope as the part where the column density slowly decreases and the external envelope as the one with a steeper decrease. The crossing point between these two envelope components defines the outer radius of the inner envelope, called R_{Infall} for reason explained in Sect. 5.2. Its values are given in Table 3.

The profile analysis is trustworthy for the central UCH II region since it is prominent and azimuthally averaged over 2π radians. The analysis is cruder for the three other H II regions

(a) column density radial profile of the central UCH II region

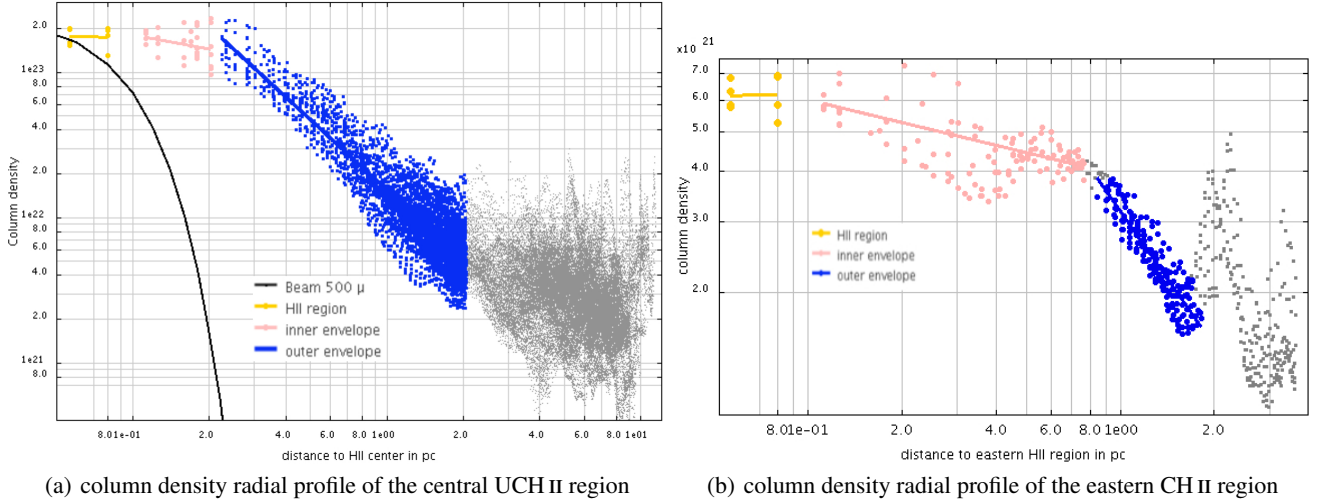(b) column density radial profile of the eastern CH II region

Fig. 6. H II region bubble (yellow line and points) surrounded by a neutral gas envelope splitting into slowly and sharply decreasing N_{H_2} parts (pink and blue lines and points). The background is defined by the lower limit of the clouds of grey points. The resolution corresponding to the *Herschel* beam at 500 μm is illustrated by the black curve in **a)**.

developing between filaments (see Fig. 2b). For these H II regions, we have selected inter-filament areas and quadrants that represent the H II regions best and avoid the ambient filamentary structure (see Fig. F.1). By doing so, we aimed to measure the contribution of the H II region envelope alone. We have checked, mainly in the case of the eastern region, that varying the azimuthal sectors selected between the major filaments does not change either the radii or the slope of the envelopes by more than 20%. However, contamination by other overlying cloud structures cannot be completely ruled out, and some studies of other isolated prominent H II regions are needed to confirm the results presented here.

The column density slopes of both the internal and the external envelopes can be represented well by power laws such as $N(\theta) \propto \theta^p$ (see Fig. 6). Since the column density is the integration of the density on the line of sight, we can logically retrieve their density profiles through measuring the column density profiles. For a single power law density $\rho(r) \propto r^q$, an asymptotic approximation leads to a very simple relation between the q index and the power law index of the column density profile described as $N(\theta) \propto \theta^p$: $q \simeq p - 1$. This assumption holds for piecewise power laws that match a large portion of the observed envelopes. It is the case of external envelopes as is confirmed in Sect. 3.5. However, for small pieces like the inner envelopes, the conversion from column density to density power law indices is more complex (see Yun & Clemens 1991; Bacmann et al. 2000; Nielbock et al. 2012).

Towards the centre, at an impact parameter[7] smaller than the H II region outer radius, all four density components contribute to the observed column density. Then a gradual increase in the impact parameter progressively reduces the number of the contributing density components. The four structural components of Fig. 3 were constrained, step by step, from the outside/background to the inside/H II region bubble.

We first estimated the background column density arising from the ambient cloud using both near-infrared extinction (Schneider et al. 2011) and the *Herschel* column density map (Fig. F.1). They consistently give background levels of

$A_v \sim 0.5$ mag[8] at the edge of the *Herschel* map. To minimise the systematic errors in determining the slope of the outer envelope, a 0.5 mag background was subtracted from the column density profiles. For the northern H II region, the power law slope measured for the envelope remains well-define with p possibly ranging from -0.4 to -0.5, although the background contribution to the observed column density profile is the most important.

We simultaneously estimated the power law coefficients of the two parts of the envelope from the slopes (p) measured on "background-corrected" column density profiles. We used the relation $q \simeq p - 1$ to measure the density profile slopes (q) of the outer envelope and obtain a first guess for the inner envelope. Tables 3 and 2 list some of the parameters derived from our column density structural analysis.

The outer envelope of the two compact eastern and western H II regions displays a column density index of $p_{out} \simeq -1$ with an uncertainty of 0.2 ($\sim 3\sigma$), which corresponds to a $\rho(r) \propto r^{-2}$ density law. The central UCH II region itself exhibits a steeper density gradient in its outer envelope with $q_{out} \simeq -2.5$. In practice, the uncertainties are such that the slopes are well defined within an uncertainty of about 10% or ~ 0.2, clearly allowing the distinction between $\rho(r) \propto r^{-2}$ and $\rho(r) \propto r^{-1.5}$ or $\rho(r) \propto r^{-2.5}$ power laws. This is a clear improvement from the studies made before *Herschel* from single band sub-millimetre observations (e.g. Motte & André 2001; Beuther et al. 2002; Mueller et al. 2002).

The northern H II region, whose envelope does not split into an inner and outer parts, has a decreasing density profile up to 0.8 pc with a power law coefficient of $q \simeq -1.5$.

The internal envelopes of the central, eastern, and western H II regions have a column density profile with power law coefficients $p_{in} \simeq -0.35 \pm 0.2$, but the conversion is not straigthforward and the density modelling made in Sect. 3.5 is needed to derived correct values.

---

[7] Impact parameter: radial distance from the line of sight to the centre.

[8] We used the relation by Bohlin et al. (1978) to transform *Herschel* N_{H_2} measurements into A_V values in mag unities, $A_V \simeq 10^{21}$ cm$^2 \times N_{H_2}$.

Table 2. Comparison of the properties of the neutral envelopes surrounding the four H II regions of Mon R2.

Region name	Direct fits on observed N_{H2} profiles				Calculated	Fits of reconstructed N_{H2} profiles			
	$N_{H2}(1pc)$ [cm^{-2}]	q_{out}	q_{in}	R_{Infall} [pc]	ρ_{1pc} [cm^{-3}]	ρ_{1pc} [cm^{-3}]	q_{out}	q_{in}	R_{Infall} [pc]
(1)	(2)	(3)	(4)	(5)	(6)	(7)	(8)	(9)	(10)
central	1.5×10^{22}	−2.7	−1.3	0.25 ± .05	2000. ± 200.	1900 ± 250	−2.75	−0.85 ± .35	0.3 ± .1
western	3.5×10^{21}	−1.8	−1.55	0.5 ± .1	300. ± 50.	370 ± 50	−1.9	−1.45 ± (.1)	0.5 ± .1
eastern	$4. \times 10^{21}$	−2.2	−1.3	0.8 ± .2	470. ± 50.	430 ± 50	−2.45	−.4 ± 0.2	1. ± .2
northern	$2. \times 10^{21}$	−1.5		−	125. ± 25.	105 ± 30	−1.45 ± .15		−

Notes. Columns 2−5 are directly fitted from the observed column density profiles, while Cols. 7−10 are adjusted from modelled column density profiles reconstructed from fixed density profiles. Density profile indices and infall radius Cols. 3−5 and Cols. 8−10 are defined in Sects. 3.4.1−3.5 and Fig. 3. The envelope density at 1 pc of Col. 6 is calculated with Eqs. (B.3) and (B.4) from Cols. 2−5 data, while the value given in Col. 7 is taken from the density model.
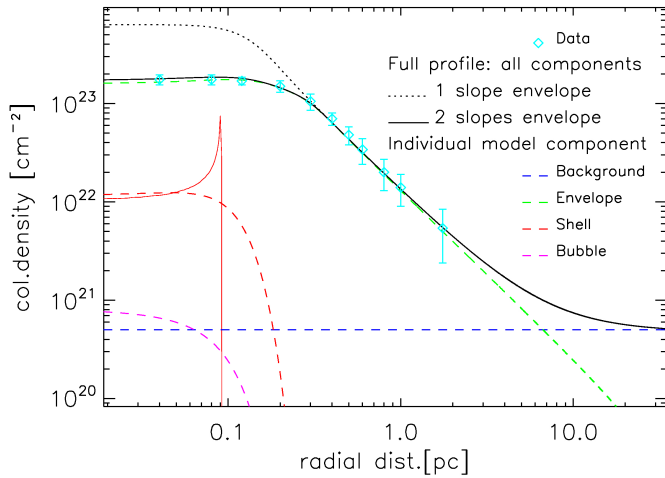

Fig. 7. Column density profile of the central UCH II region (cyan diamonds with σ errors bars) compared to models with all components illustrated in Fig. 3. The neutral envelope with two density gradients or with a single one are shown by a black line and a dotted black line respectively. An envelope model with a single density gradient cannot match the observed data. Individual components after convolution by the beam are shown by magenta, red, green, and blue dashed lines, for the bubble, shell, envelope and background. The continuous red line shows the unconvolved shell profile at an infinite resolution.

Fig. 8. Column density profile for northern H II region and its four components coded with the same colours as in Fig. 7. The dotted green line corresponding to the sum of the envelope and background contributions matches well with observed data.

3.5. Density modelling

We here perform a complete modelling of the observed column density profiles to adjust and evaluate the relative strength and the characteristics of the components used to describe H II regions and their surroundings. We modelled four different components along the line of sight to reconstruct the observed column density profile. We used the size and density profiles derived in previous sections and listed in Table 3 to numerically integrate between proper limits, along different lines of sight, the radial density profiles of the background, envelope (external then internal), H II region shell, and bubble. For a direct comparison with observed profiles, we convolved the modeled column density profiles with the 36″ resolution of the *Herschel* N_{H2} maps. Figures 7, 8 display the calculated column density profiles of each of the four aforementioned structural components and the resulting cumulative profile. Figure F.1 also locates, with concentric circles, the different components used to constrain the structure of the central UCH II region.

We recall that the background is itself defined as a constant-density plateau: $A_V \sim 0.5$ mag for all H II regions. The
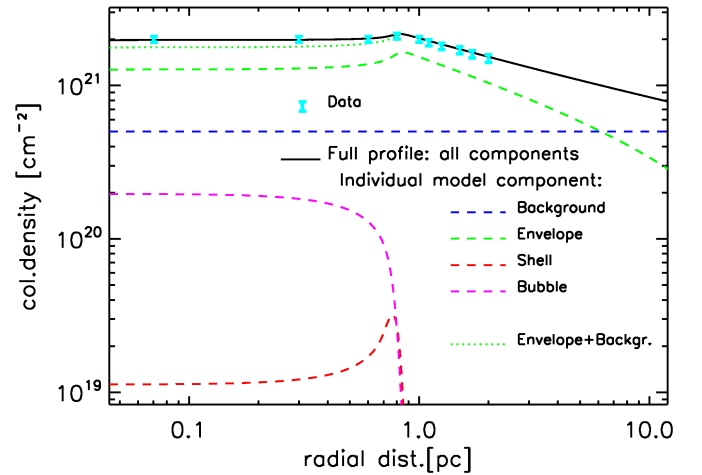
background, even if faint, has an important relative contribution towards the outer part of the H II region structure, where the envelope reaches low values. For the northern H II region, the background contribution to the observed column density profile is almost equal to that of the envelope, as it can be seen on the reconstructed profile of Fig. 8.

Our goal is to estimate for each of the four H II regions in Mon R2, the absolute densities of the envelope, shell, and H II region bubble (see Tables 1−3).

We adjusted our model to the complete column density profile, progressively adding the necessary components: outer envelope, inner envelope, shell and bubble, the latter first assumed to be empty. In Table 2 we compare the results directly obtained from observationnal data and from data modelling.

We first modeled the density profile observed at radii greater than 1 pc, dominated by the outer envelope density. We jointly adjusted the density at 1 pc, ρ_1 and the density power law slope, q_{out}. The q_{out} values derived from the $q = p - 1$ relation are in excellent agreement with the fitted ones. The ρ_1 values obtained are very similar to those calculated with Eqs. (B.3) and (B.4) from the column density values at 1 pc and the appropriate q_{out} values. Our results prove that the asymptotic assumption is correct for the outer envelope component. The characteristics of the inner envelope, which are mixed on the line of sight with those of the outer envelope, is only reachable through

Table 3. Properties of the neutral envelopes surrounding the four H II regions of Mon R2.

Region name	R_{Infall} [pc]	R_{out} [pc]	$\rho(r) \propto r^q$		Infall age [Myr]	$N_{\text{H2}}^{\text{Max}}$ [cm^{-2}]	R_{HM} [pc]	$\langle \rho_{\text{obs}} \rangle$ [cm^{-3}]	$\rho_{\text{env}}(1\text{pc})$ [cm^{-3}]	$\rho_{\text{env}}(R_{\text{H II}})$ [cm^{-3}]
			q_{in}	q_{out}						
(1)	(2)	(3)	(4)	(5)	(6)	(7)	(8)	(9)	(10)	(11)
central	$.3 \pm .1$	$2.5 \pm .5$	$-.85 \pm .35$	-2.7	$.5-1.5$	$2. \times 10^{23}$	0.35	1.4×10^5	2000 ± 300	1.5×10^5
western	$.5 \pm .1$	$3. \pm 1.$	$-1.5 \pm .15$	-1.8	$.8-2.5$	$16. \times 10^{21}$	0.4	$9. \times 10^3$	350 ± 50	12000
eastern	$.9 \pm .2$	$2.5 \pm 1.$	$-.4 \pm .2$	-2.3	$1.4-4.4$	$7. \times 10^{21}$	0.9	1.6×10^3	450 ± 50	1200
northern	>2	$2.5 \pm .5$	$-1.45 \pm .15$	$-$	$>3.-10.$	$3. \times 10^{21}$	1.5	300.	115 ± 30	150

Notes. Columns 2−5 describe the density profile of the neutral envelopes surrounding H II regions by listing the radius separating the inner and outer envelope components, the outer radius, and the density power law slopes of the two envelope components. Uncertainties (3σ) on q_{out} are estimated to be 0.2. Column 6 gives the time elapsed since the beginning of infall and protostellar collapse. It is calculated from R_{Infall} (Col. 2) and Eq. (11) with a velocity range from one to three times the sound speed (see Sect. 5.2) and has a statistical error of 20%. Columns 10−11 give the absolute values of the density measured at $r = 1$ pc and at the $R_{\text{H II}}$ radius, from the complete modelling of column density profiles (see Sect. 3.5). Column 11 is used to estimate, through Eq. (4), the mean initial neutral gas density before the ignition of an H II region.

modelling. Figures 7, 8 show that once the envelope density structure is fixed, the modelled column density profile fits the observed one for radii larger than $R_{\text{H II}}$ nicely.

The shell and the bubble are expected to have a weak influence on the profiles of the ultra-compact-to-compact H II regions (here the central, eastern, and western regions). Indeed, the H II bubble sizes and the amount of gas mass collected in the shell are so small that their contribution can be almost neglected, and high resolution would be needed to observe the narrow shoulder enhancement at the border of the shell (see Fig. D.1). These two components are, however, definitely needed to reproduce the central column density of the more extended and diffuse, northern Extended H II region. Figure 8 displays an inner column density plateau and a tentative shoulder of the column density profile just at the $R_{\text{H II}}$ location. We have estimated an upper limit to the mean density, column density, and mass for the northern H II region swept-up shell, assuming a 0.01 pc thickness with a density varying from 50 to 1000 cm^{-3}: $N_{\text{H2}}^{\text{shell}} \sim 1.6 \times 10^{19}$ cm^{-2}, and 3 $M_\odot$. This putative shell is, however, difficult to disentangle from the envelope border and the complex cloud structure in this area.

According to Hosokawa & Inutsuka (2005), the central bubble should be devoid of cold dust in the earliest phase of H II region development, roughly corresponding to the compact H II phase. In the case of the central UCH II region, we used the electron density of 1.6×10^3 cm^{-3} (Quireza et al. 2006) as an upper limit for the H II bubble density of neutral gas. Even this relatively high density value results in a negligible contribution to the modelled column density profile (see Fig. 7). For the northern H II region, a low-density ($\sim$50 cm^{-3}) central component needs to be introduced in the bubble to reconcile the modeled profile and the observational data. Without it, we would observe a relative hole or depletion in the centre of the column density profile (see red and green lines in Fig. 8 compared to cyan or black ones). The uncertainties are such that the exact value of the inner density component of the northern H II region is not known better than to a factor of ten. Therefore, our modelling can only give upper-limit densities for the bubble gas content and H II region shell.

Table 3 lists the adopted values of the envelopes density characteristics. The envelope density at 1 pc radius, i.e. $\rho_{\text{env}}(r = 1\text{ pc})$, which was used to scale the parametrised density profile, defines the absolute level of density in the envelope. It also gives the density observed at the inner border of the envelope, i.e. $\rho_{\text{env}}(r = R_{\text{H II}})$, corresponding to the maximum value measured now in the envelope. The central density of the eastern Compact H II region is a bit weak and atypical. For the northern

H II region, the inner border of the envelope is at $R_{\text{H II}} \sim 0.8$ pc, and we can extrapolate the $\rho(r) \propto r^{-1.5}$ density profile to a distance of 0.1 pc: $\rho_{\text{estimated}}(r = 0.1$ pc$) \sim 6.6 \times 10^3$ cm^{-3}. We also considered the density at much smaller radii, which would correspond to the inner radius of the extrapolated protostellar envelope and the central core density: $\rho_{\text{env}}(r = 0.005$ pc/1000 AU), Col. 4 in Table 4.

All inner envelopes have a power law slope that is smaller than or equal to the expected infall value of 1.5. The values lower than 1.5 could be due to sub-fragmentation in the inner envelope. Some indications of inhomogeneous clumpy structures are indeed revealed by high-resolution maps (Rayner et al., in prep.). All outer envelopes have power law slopes greater than or equal to the expected SIS value of 2, corresponding to hydrodynamical equilibrium. The high value observed for the central H II region could be due to additional compresion (Sect. 5.1, Appendix C). All these density determination will be used below to estimate the mean initial neutral gas density before the ignition of an H II region.

4. Ionisation expansion time

The physical characteristics presented in the previous sections are used here to constrain the expansion time of the ionisation bubble in its neutral envelope. In Sect. 4.1, analytical calculations without gravity show that the average initial density, $\langle \rho_{\text{initial}} \rangle$, is the main parameter dictating the expansion behaviour. In Sect. 4.2, simulations are compared to analytical results of Sect. 4.1 to determine the impact of gravity on expansion. In constant high-density envelopes, gravity prevents expansion through quenching or re-collapse, but in a decreasing-density envelope, the impact of gravity becomes negligible once the expansion has started. We thus conclude in Sect. 4.3 that analytical calculations without gravity can be used to derive valid ionisation expansion times.

4.1. Strömgren-sphere expansion analytical calculations

Differences in size between the northern and the western H II regions, which harbour an exciting star of the same spectral type, tend to suggest that the northern H II region is more evolved than the western one (see Fig. 2a and Table 1). The larger number of striations observed in the visible image of the northern reflection nebula also indicate an older stage of evolution (Thronson et al. 1980; Loren 1977).

To confirm these qualitative statements, we here determine time differences in the beginning of the ionisation expansion

H II regions for the four H II regions. We recall that the deeply embedded central UCH II region has no optical counterpart, while the western, eastern, and northern H II regions are respectively associated with the vdB67, vdB69, and vdB68 nebulae.

4.1.1. Average initial density

The density observed at the inner border of the envelope (i.e. $\rho_{env}(r = R_{H\,II})$, corresponding to the maximum value measured now in the envelope) can be used to estimate the density the protostellar envelope had at the time of the ignition of the ionisation, when averaged within a sphere of $R_{H\,II}$ radius. Given the inner density structure observed for the four H II regions envelopes, whose density gradient is described by $\rho(r) \propto r^{q_{in}}$, the mean density of the initial envelope part, which is now mostly collected in the shell, is given by

$$\langle \rho_{initial} \rangle_{R_{H\,II}} = \left(\frac{3}{3 - q_{in}} \right) \times \rho_{env}(r = R_{H\,II}) \qquad (4)$$

and derived in Appendix A.1. It is the most important parameter for analytical calculations, and its calculated values are given in Col. 2 of Table 4.

4.1.2. Expansion in an homogenous density static envelope

Spitzer (1978) predicted the expansion law of a Strömgren sphere and thus the evolution of the H II region size with time in an homogeneous medium (see also Dyson & Williams 1980 and Arthur et al. 2011, Eq. (1)). Following Ji et al. (2012), we inverted the relation and expressed time since the ignition of the ionisation as a function of the observed H II region radius, $R_{H\,II}$:

$$t_{Spitzer}(R_{H\,II}, \langle \rho_{initial} \rangle) = \frac{4}{7} \times \frac{R_{Str}}{c_s} \left[\left(\frac{R_{H\,II}}{R_{Str}} \right)^{7/4} - 1 \right], \qquad (5)$$

where $c_s = 10$ km s^{-1} is the typical sound speed in ionised gas, and R_{Str} is the radius of the initial Strömgren sphere (Strömgren 1939, 1948). The latter is given by the following equation

$$R_{Str} = \left(\frac{3 N_{Lyc}}{4 \pi \alpha_B \langle \rho_{initial} \rangle^2} \right)^{1/3}, \qquad (6)$$

or in numerical terms

$$R_{Str} \simeq 301 \, \text{AU} \left(\frac{N_{Lyc}}{10^{47} \, \text{s}^{-1}} \right)^{1/3} \left(\frac{\langle \rho_{initial} \rangle}{10^6 \, \text{cm}^{-3}} \right)^{-2/3} \qquad (7)$$

where $\langle \rho_{initial} \rangle$ is the initial mean density in which the ionisation occurs, N_{Lyc} is the number of hydrogen ionising photons from Lyman continuum and $\alpha_B = 2.6 \times 10^{-13}$ cm^3 s^{-1} is the hydrogen recombination coefficient to all levels above the ground.

The ionisation ages determined from Eq. (5) strongly depend on the mean initial density, $\langle \rho_{initial} \rangle$ (see its definition in Sect. 4.1.1), since it defines the initial radius of the ionised sphere, R_{Str} (see Eq. (6)). With the assumption that the expansion develops in a constant-density medium, the ionisation age is strictly determined by the initial and present sizes of the ionised region, R_{Str} and $R_{H\,II}$ (see Eq. (5)).

Initial density estimates are very uncertain since they depend on assumptions made for the gas distribution before protostellar collapse and its evolution conditions. Nevertheless, the envelope density structure can be approximated by the mean density of the envelope part, which was travelled through by the ionisation front expansion and has been collected in the shell.

Considering the maximum density of the different H II region envelopes at their inner border ($R_{H\,II}$) and using Eq. (4), we calculate an initial mean density ($\langle \rho_{initial} \rangle_{H\,II}$) reported in Col. 2 of Table 4. Assumed to be representative of an envelope with an equivalent homogenous constant density, this value is jointly used with the ionising flux given in Table 1 to calculate the corresponding expansion time with Eq. (5) and is given in Col. 3 of Table 4. The expansion time of compact and UCH II regions are similar ($t_{Exp} \sim 20-90 \times 10^3$ yr) with a range that is mainly due to different initial densities. The northern extended H II region is three to 15 times older ($\sim 300 \times 10^3$ yr), in line with what is expected from their size differences.

4.1.3. Expansion in a density decreasing static envelope

The present study shows that H II regions develop into protostellar envelopes whose density decreases with radius (see Sect. 3.5, see also introduction in Immer et al. 2014). The equation given by Spitzer (1978) describing their expansion in a medium of homogeneous density (Eq. (5)) therefore does not directly apply. We calculated the expansion of an ionised bubble in an envelope with a density profile following a power law. We included in this envelope a central core with a r_c radius and a constant density of ρ_c. The clump density structure thus follows

$$\rho = \begin{cases} \rho_c & \text{for} & r \leq r_c \\ \rho_1 \times r^{-q} & \text{for} & r > r_c \\ & \text{with } \rho_c = \rho_1 \times r_c^{-q} \end{cases} \qquad (8)$$

where ρ_1 is the density at 1 pc deduced from the constructed density profile or directly measured from the column density at the same radius (see Sect. 3.5). The expansion as a function of time in a decreasing envelope is derived by calculations detailed in Appendix A.2. In close agreement with previous work by Franco et al. (1990), it is given by

$$t_q(R_{H\,II}) = \frac{4}{7 - 2q} \times \frac{r_c^{7/4}}{R_{Str}^{3/4}} \frac{1}{c_s} \left[\left(\frac{R_{H\,II}}{r_c} \right)^{7-2q/4} - 1 \right] \qquad (9)$$

$$= \frac{4}{7 - 2q} \times \frac{r_c}{V(r_c)} \left[\left(\frac{R_{H\,II}}{r_c} \right)^{7-2q/4} - 1 \right]$$

with the same definitions as in Eqs. (5), (6) and where $V(r_c) = (R_{Str}/r_c)^{3/4} \times c_s$ is the shell expansion speed at the homogeneous core radius r_c. For a constant density, which is the Spitzer case, $q = 0$ and $r_c = R_{Str}$, and Eq. (9) resumes to Eq. (5).

The inner envelope density profiles of the four regions have gradients which at most corresponds to the free-fall case, with a power law coefficient of $q \lesssim 1.5$. For higher values ($q > 1.5$), Franco et al. (1990) showed that expansion is in the so-called "champagne" phase. In such cases, there is neither velocity damping nor creation of a collected shell (see also Shu et al. 2002; Whalen & Norman 2006). In contrast, the shell and low expansion velocity observed for the central UCH II region (Fuente et al. 2010; Pilleri et al. 2012, 2013, 2014) indicate that $q = 1.5$ is probably an upper limit. The ionisation front should then stay behind the infall wave, $R_{H\,II} < R_{Infall}$, with the expansion starting at supersonic velocities, classically ~ 10 km s^{-1}, but then quickly damped to values around the sound speed in the neutral molecular medium. As a matter of fact, the expansion of the central UCH II slowed down to ~ 1 km s^{-1} at $\sim 0.08/0.09$ pc (Pilleri et al. 2014, and references therein), so far behind the infall wave situated around 0.3 pc (see Table 3). More generally, in the case of the four H II regions of Mon R2, even if the initial

Table 4. Estimations of expansion time for the four H II regions of Mon R2.

Region	Analytical calculations and simulations without gravity					Simulations with gravity		Dec. density	Adopted expansion time
	constant density		decreasing density			constant density			
	$\langle\rho_{\text{initial}}\rangle$ [cm^{-3}]	$t_{S\,pitzer}$ [kyr]	ρ_c [cm^{-3}]	t_{exp} (calc) [kyr]	t_{exp} (simu.) [kyr]	$\langle\rho_{\text{initial}}\rangle_{\text{Max}}$ [cm^{-3}]	t_{exp} (simu) [kyr]	t_{exp} (simu) [kyr]	time [kyr]
(1)	(2)	(3)	(4)	(5)	(6)	(7)	(8)	(9)	(10)
central	2×10^5	54	2×10^6	58	53	1.7×10^5	133	–	90 ± 40
western	2.4×10^4	92	1×10^6	108	98	1.7×10^4	215	–	150 ± 50
eastern	1.5×10^3	23	4×10^3	24	23	8×10^3	170	24	25 ± 5
northern	3×10^2	310	2.5×10^5	370	355	5×10^3	3700.	370	350 ± 50

Notes. (2) average initial density derived from Eqs. (4) and (10). (3) Expansion time calculated from Eqs. (5) and (6) and using the average density of Col. 2. (4) Constant density of central core derived from Eq. (8) with $\rho_c = 0.005$ pc. (5) Expansion time calculated from Eqs. (9) and (6) and using the central density of Col. 4. (6) Expansion time derived from simulations without gravity using a decreasing-density envelope extrapolated up to the central density (Col. 4). Considered as a lower limit (see introduction of Sect. 4.2). (7) Maximum constant density allowing ionisation expansion in simulations with gravity, (see Sect. 4.2.2). (8) Expansion time calculated by simulations using the maximum constant density of Col. 7. Considered as an upper limit. (9) Expansion time derived from simulations with gravity using a decreasing-density envelope extrapolated up to highest possible central density (see Sect. 4.2.3). (10) Adopted expansion time (see Sects. 4.2.4 and 4.3). Errors do not take any systematic effects into account, such as those due to small-scale non-3D geometry or density inhomogeneity.

ionisation extension exceeded the central core size $R_{\text{Str}} > r_c$, ionisation would expand in internal infalling envelopes with shallow ($q < 1.5$) density profiles. The ρ_1 value used in Eq. (8) corresponds to the internal envelope, $\rho_{\text{int}}(1\text{pc})$, and is calculated from the one observed in the external envelope, $\rho_{\text{env}}(1\text{pc})$, by the relation

$$\rho_{\text{int}}(1\text{ pc}) = \rho_{\text{env}}(1\text{ pc}) \times R_{\text{Infall}}^{(q_{\text{in}}-q_{\text{out}})} \qquad (10)$$

where $\rho_{\text{env}}(1\text{ pc})$, R_{Infall}, q_{in}, and q_{out} are given in Table 3.

For the central core, we adopted a size of 0.005 pc (~1000 au), which is meant to represent the size where the spherical symmetry is broken. Since 3D effects are beyond the scope of this paper, gas on small scales (<0.005 pc) is represented by an homogeneous and constant density medium. This value is between the typical size of Keplerian disks surrounding low-mass pre-main sequence T Tauri stars (~0.001 pc, 200 au, Carmona et al. 2014; Maret et al. 2014; Harsono et al. 2014) and the largest disks or flattened envelopes observed around intermediate- to high-mass Herbig Ae-Be stars (0.01 pc, 200−2000 au, Chini et al. 2006; de Gregorio-Monsalvo et al. 2013; Jeffers et al. 2014). Calculations with various r_c values in the conditions considered here ($q \lesssim 1.5$) show that when $r_c \ll R_{\text{H II}}$, the value of r_c does not have much influence on the expansion time of the ionised bubble.

For objects studied here, the initial size of the Strömgren sphere, R_{Str}, is always smaller than the core radius, r_c. Therefore the expansion is decomposed in two phases: the expansion in an homogenous medium of constant density, ρ_c from R_{Str} up to r_c and the expansion in the decreasing density part of the envelope between r_c and $R_{\text{H II}}$. The expansion time of the first phase in the central core, t_c, is given by the Spitzer formula (Eq. (5)), and the second phase in the decreasing density envelope, t_d, is given by Eq. (9). The total expansion time $t_{\text{exp}} = t_c + t_d$, is given in Col. 5 of Table 3. It is consistent with the value obtained for an expansion within a homogenous-density medium with an equivalent mass (see Col. 3), corroborating the constant-density equivalence hypothesis and the calculation performed in Sect. 4.1.2. Agreement is better for the compact or UCH II regions, which have $\langle\rho_{\text{initial}}\rangle$ closer to ρ_c than the extended northern region.

The time for an H II region to expand depends strongly on the density gradient in the inner envelope through the density extrapolated for the 0.005 pc core, ρ_c, which determines the Strömgren radius, R_{Str}. The gradient index, q_{in}, itself gives the transit time in

the envelope, t_d. All measures are uncertain, especially because the H II region expansion occurred in an envelope whose density may be higher than the one presently observed. If ionisation expansion took place in a primordial envelope with a density slope typical of free-fall, $q_{\text{in}} = 1.5$, then the calculations would give a minimum age of 10^5 yr for all three compact and UCH II regions.

4.2. Simulations of H II regions development with gravity

We used dedicated simulations to assess the impact of a decreasing density and the effect of gravity on our estimates of the ionisation expansion time. We employed the HERACLES[9] code (e.g. González et al. 2007), which is a three-dimensional (3D) numerical code solving the equations of hydrodynamics and which has been coupled to ionisation as described in Tremblin et al. (2012a,b). The mesh is one dimensional in spherical coordinates with a radius between 0 and 2 pc and a resolution of 2×10^{-3} pc, corresponding to 10 000 cells. The boundary conditions are reflexive at the inner radius and allow free flow at the outer radius. The adiabatic index γ defined as $P \propto \rho^{\gamma}$ is set to 1.01, allowing us to treat the hot ionised gas and the cold neutral gas as two different isothermal phases.

The effects considered here are 1) the ionisation expansion and 2) the gravity of the central object. The envelope is considered at rest at the beginning of the simulation, but when gravity is taken into account the infalling part of the envelope has a velocity close to the expected values.

Our models consider the gravitational effects of the ionising star but not that of the whole cloud, which could collapse under its own gravity. Such gas infall is important but modelling it is beyond the scope of this paper. It requires complex 3D turbulent simulations with self-gravity such as those developed in Geen et al. (in prep.). Their main conclusion is that global cloud infall can stall the expansion of H II regions but do so less efficiently than 1D arguments. Indeed, infall gas should generally be inhomogeneous and clumpy, and the H II region should expand in directions where fewer dense clumps are present.

Realistic winds from early B type stars have been checked to make certain they do not quantitatively modify the ionisation expansion time. A wind cavity in the ionised gaz would indeed only marginally increase the electronic density.

---

[9] Available at http://irfu.cea.fr/Projets/Site_heracles

Important leaking and outflows of ionised matter would have a noticeable impact and is observed neither in the temperature map as seen by Anderson et al. (2015) for RCW120 nor in the hydrogen RRL or the radio data. Disruption of the molecular cloud thus cannot be important in the UCH II region. Moreover, the ionising photon flux we used comes from the H II region cavity. Any leaking of ionised matter would decrease the amount of ionised gaz in the cavity and thus increase the expansion time.

Complex structure and motions of the ionised gas have been reported by Jaffe et al. (2003) and modelled by Zhu et al. (2005, 2008). They argue for tangential motions of the ionised gas along the surface of the H II region, which cannot suppress the thermal pressure at the origin of the expansion evolution. Thermal turbulence of ionised gas, the prime driver of expansion, is taken into account in simulations. Recent works show that introducing additional turbulence does not affect the H II region expansion much because it would only increase the expansion time weakly (see Arthur et al. 2011; Tremblin et al. 2012a, 2014b).

Taking all these complexities and secondary effects into account is beyond the scope of the present paper since we merely tried to reproduce an overall behaviour, using the mean density at the origin. Detailed studies would require to take departure from spherical symmetry on small scales into account.

Simulations are based on 1) the density profiles derived from column density and 2) UV ionizing fluxes deduced from radio data. Temperature or electronic density are not used in the initial conditions so any changes of their values would not affect the simulation results.

For comparison, we used the profiles presented in Sect. 4.1.3 to perform simulations of H II regions expanding within decreasing density envelopes without taking the gravity into account. The results given in Col. 6 of Table 4 agree within 15% with analytical calculations given in Col. 5. The remaining differences arise from assumptions made in the analytical solutions, which neglect the inertia of the shell and strong external pressure. These expansions are illustrated in Figs. 10, 11 by black lines.

We hereafter investigate the effect of gravity. Section 4.2.1 shows that extrapolating density profiles as done for analytical calculations of Sect. 4.1.3 would lead to quenching or recollapse for the central, western, and northern H II regions. For the eastern region, the extrapolated low central density is not high enough for gravity to impede expansion, so expansion time remains similar. In Sect. 4.2.2, we calculate the maximum constant-density medium inside which the H II regions could develop. Unrealistic envelope models with constant density would induce re-collapse even on a large scale, but they nevertheless provide useful upper limits to the ionisation expansion time. The case of the less dense northern and eastern H II regions is discussed again in Sect. 4.2.3, and we confirm that once the expansion starts, the gravity influence is negligible, at least in decreasing-density envelopes. In Sect. 4.2.4, we summarise the results we obtained from simulations and give estimates of the ionisation expansion time for the four H II regions in Mon R2.

4.2.1. Effect of gravity: quenching or recollapse

Introducing gravity due to the central object in the simulations results in the quenching (also called "choke off" by Walmsley 1995) of three H II regions discussed here, and they expand in high-density media: central, western, and northern regions. They cannot develop and are quenched or gravitationally trapped

(Keto 2007), even with the introduction of a realistic wind support arising from early B-type stars.

The eastern H II region is not quenched and can develop in the observed inner envelope, which has a weak density gradient. The values of $\langle \rho_{\text{initial}} \rangle$ and even ρ_{c} are lower than the maximum constant density $\langle \rho_{\text{initial}} \rangle_{\text{Max}}$ (see Table 4), explaining why quenching is not occurring here. In this case of a low-density envelope, the expansion time obtained in simulation without gravity (23 kyr, see Col. 6 of Table 4) is identical when including gravity in simulation (24 kyr, see Col. 9 of Table 4).

To allow expansion of the three H II regions quenched in simulations, one needs to decrease the central density of the profile, ρ_{c}. If we keep extrapolating the density profile observed for the outer envelope (see ρ_1 in Col. 10 of Table 3), the only way is to increase the constant density core radius, r_{c}. This determines the maximum central density value, $\rho_{\text{c}}^{\text{Max}}$, and the corresponding minimum core radius, $r_{\text{c}}^{\text{min}}$, allowing an H II region to develop up to the observed size. For the UC (central) and the compact (western) H II regions, $r_{\text{c}}^{\text{min}}$ is larger than $R_{\text{H II}}$, corresponding to an expansion in a homogenous medium of density $\rho_{\text{c}}^{\text{Max}}$. The highest density observed in the envelope at a radius corresponding to the H II region size is thus greater than the maximum density allowed by this scenario, $\rho_{\text{c}}^{\text{Max}} < \rho(R_{\text{H II}})$, and the radii of constant density are larger than the actual H II region sizes, $r_{\text{c}} > R_{\text{H II}}$. Even if these assumptions are unrealistic, they are useful to determine upper limits. Another way to reduce the central density, as shown in Eq. (8), is to keep the same central core radius but decrease the density of the entire profile through the ρ_1 value. This configuration implicitly assumes a mean envelope density at the initiation of the H II region expansion that is lower than expected.

Figure 10 shows four simulations for the central UCH II region. The expansion in a decreasing-density envelope with no gravity (black lines) is compared to two simulations including gravity and occurring in constant-density envelopes. For a constant low-density envelope (cyan curve) expansion can reach the observed H II region size. For higher constant density (red dashed curve), the re-collapse occurs earlier and closer, preventing the expansion up to its present size. Increasing the density gradient of the inner envelope from that presently observed ($q_{\text{in}} = 0.85$, continuous black line) to that expected for free-falling gas ($q_{\text{in}} = 1.5$, dotted black line) increases the extrapolated density and thus the expansion time.

Figure 11 gives the expansion behaviour of five simulations for the northern H II region. As in Fig. 10 and with the same colours, three simulations describe expansion within a decreasing density envelope without gravity (black line) and expansion in constant high- and low-density envelopes without gravity (dashed red and continuous cyan curves, respectively). Two additional simulations in a decreasing density envelope with gravity are displayed by a blue line for the nominal average initial density and a dashed blue line for a lower density.

Figure 9 shows the velocity field of a simulation for the northern region obtained at three different times. The simulation includes the gravity of the central ionising object in a density decreasing envelope with a central core of 0.05 pc and a density of 110 cm^{-3} at 1 pc. This envelope has a mean density in agreement with the observed characteristics (see Table 3). It corresponds to the blue continuous curve in Fig. 11. The gravity influence is only noticeable at small scales where gas velocity is negative corresponding to infall, proeminent mainly in the ionised bubble. The effect is less pronounced outside the shell and get weaker when the H II region size increases.
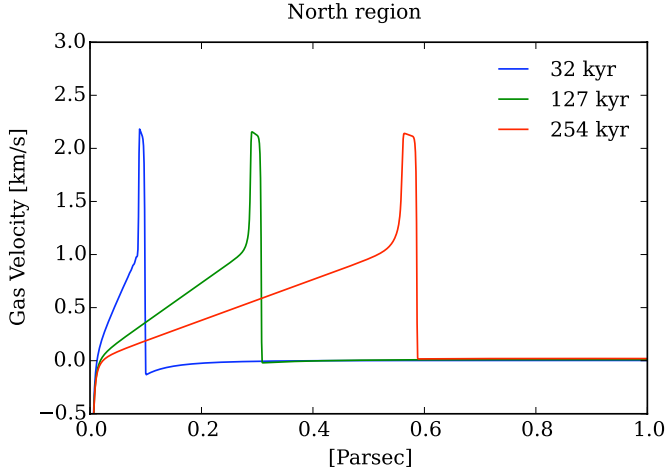
North region

Fig. 9. Velocity field from numerical simulations for the northern H II region expansion at three different times. Simulation is made with gravity and in an envelope of decreasing density, which is extrapolated from the observed one up to a constant density within $r_c = 0.005$ pc.
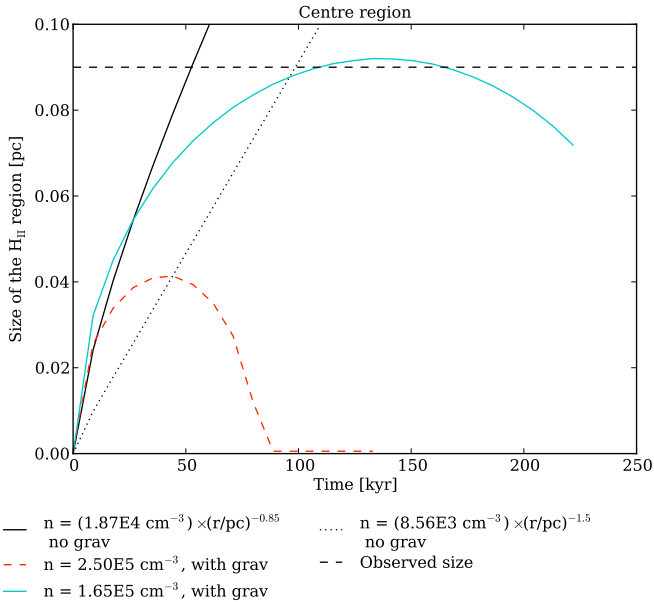
Centre region

Fig. 10. Numerical simulations for the central UCH II region expansion. In black: without gravity and in an envelope of decreasing density, which is extrapolated from the observed one up to a constant density within $r_c = 0.005$ pc. In dotted black: without gravity in an envelope of decreasing density with a gradient typical of infall, $\rho \propto r^{-1.5}$. In cyan: with gravity and in an envelope with a constant density of 1.65×10^5 cm^{-3}, just allowing the observed size to be reached (black dashed line). In dashed red: with gravity and in an envelope with a constant density of 2.5×10^5 cm^{-3}, collapses again before reaching the observed size.

4.2.2. Case of constant-density envelopes

We simulated the expansion in a constant density envelope, whose value could be compared to the initial average density of the envelope material swept up by the expansion. The latter is estimated through Eq. (4) (see Col. 2 of Table 4). This approach is validated in the case of the northern region (see Sect. 4.2.3) and is shown to be a good approximation for all H II regions since, for analytical calculations without gravity, the expansion times given in Cols. 3 and 5 of Table 4 are similar.

The central UCH II region and the western compact H II region are quenched by gravity when densities approach the initial average density extrapolated from the observed envelope. For these two regions, we thus decreased the envelope average density until their H II regions develop and reach their actual size. The associated expansion times are then upper limits measured for the densest, homogeneous, and constant density envelopes. Any density above this value would result in quenching or re-collapse before reaching the observed size. Any configuration that allows expansion up to the observed size leads to a shorter expansion time. The corresponding maximum values of the initial homogeneous constant density and expansion time are given in Cols. 7−8 of Table 4.

Figure 10 shows the effect of gravity on the expansion for the central UCH II region in a constant low-density envelope (cyan curve) compared to the expansion in a decreasing density envelope constrained by observational data, but without gravity (black line). For higher density (red dashed curve), the re-collapse occurs, preventing the expansion to reach the observed size. The same re-collapse behaviour is observed for the western compact H II region. At the beginning of the expansion, corresponding to small scales, gravity can have a strong influence. In the case of a constant-density envelope, the collected mass noticeably increases when size grows. The re-collapse of the shell is thus favoured in a constant-density envelope, but it occurs less easily in a more realistic, decreasing-density envelope or at larger size. At the beginning of the expansion, the expansion is faster, even with gravity, in the constant-density cases. This arises from the fact that the central density here is much lower than in the case without gravity of extrapolated envelopes with decreasing density. When the collected mass becomes important, the expansion is strongly slowed down by gravity and even stops. Re-collapse then occurs, at large distance, but a constant density is unrealistic for such large sizes.

The northern H II region could expand up to its observed size in an envelope with a maximum constant density of 5×10^3 cm^{-3}. This density is much higher than the mean value extrapolated from observations, and the observed size would be reached in a very long and unlikely time of at least 3×10^6 yr. At this large distance, re-collapse will not occur. More realistically, the northern H II region should have expanded in an envelope with constant density of 300 cm^{-3} (cyan curve in Fig. 11), equal to the initial average density deduced from the envelope presently observed. This gives an expansion time of $\sim 300 \times 10^3$ yr. As for the central UCH II region, the constant-density envelope case has a low density at the centre. which favours the expansion at the beginning (cyan curve). But on large scales the expansion times of all models calculated for the nominal constant average density envelope converge to similar values. The same situation applies to the eastern H II region. Better estimates of the expansion time can be obtained for the northern and eastern H II regions, as shown in the Sect. 4.2.3.

4.2.3. Case of decreasing-density envelopes

The two options already mentioned in Sect. 4.2.1 for reducing the central density are suitable for the northern H II region. The first option is to increase the radius of the constant density core, r_c. The lower density and larger size of the northern region allows expansion with gravity without quenching up to the H II region size. Nevertheless, the required size of the central core, $r_c \sim 0.05$ pc (10 000 au), is then much larger than those inside which we expect a departure from the spherical symmetry (~ 0.001 pc/200 au−0.005 pc/1000 au). As in the case of a
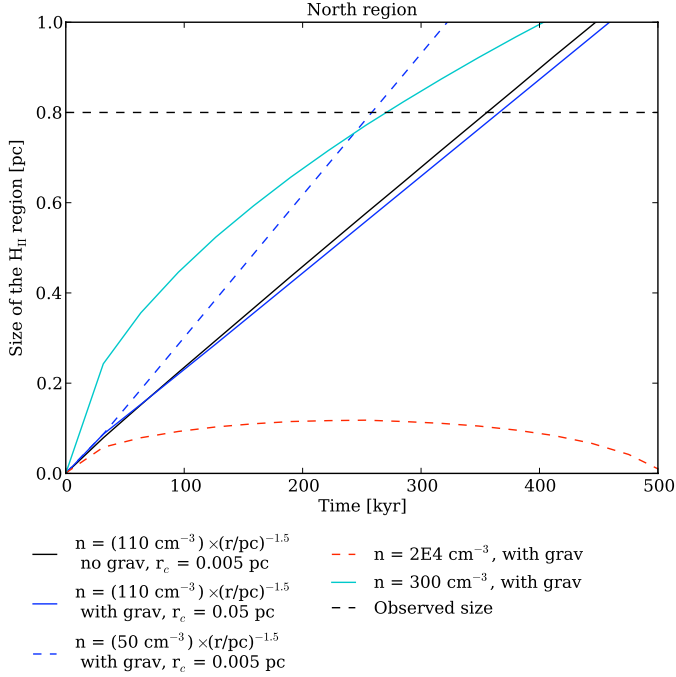
Fig. 11. Numerical simulations for the northern H II region. Simulations with and without gravity are in colours and black, respectively. Continuous lines correspond to simulations with similar average initial density, $\langle\rho_{\mathrm{initial}}\rangle = 300$ cm^{-3}. The envelope has a decreasing power-law density with the characteristics of the observed one and extrapolated to a constant core of radius 0.005 pc (black) and 0.05 pc (dark blue). For the blue dashed line, the envelope has a power law decreasing density with an index corresponding to the observed gradient but with a 50 cm^{-3} density at 1 pc extrapolated to a constant core at 0.005 pc. For the cyan and red dashed curve, the envelope has a constant density of 300 cm^{-3} (cyan), corresponding to the average initial density, or a higher 2×10^4 cm^{-3} density (red dashed), leading to re-collapse.

constant-density envelope, the initial conditions and the central structure of the H II region has less of an impact on the analysis of the old and more developed northern H II region since the expansion has already taken place for a longer time. This explains why the expansion times are not very different with and without gravity (blue and black continuous lines in Fig. 11). The highest central density allowing an H II region expansion up to the observed size defines the maximum time of 370×10^3 yr (see Col. 9 of Table 4).

The second option is to lower the density of the overall structure, and in the northern H II region case, a factor of two is necessary. The density thus decreased by 2, the expansion time is noticeably reduced as shown in Fig. 11 by the blue dashed line. From Eq. (9) ($t_{\mathrm{exp}} \propto R_{\mathrm{Str}}^{-3/4}$) and Eq. (6) ($R_{\mathrm{Str}} \propto \rho^{-2/3}$), the expansion time relates to density through its square root: $t_{\mathrm{exp}} \propto \rho^{1/2}$. This agrees with the time approximately divided by $\sqrt{2}$ between the two cases, ρ_1 and $\rho_1/2$ (blue and blue dashed lines in Fig. 11).

In fact the average initial density, $\langle\rho_{\mathrm{initial}}\rangle$, is identical for the three cases best representing the northern region. Case 1 is the first option mentioned above in this section with gravity and an enlarged central core (blue line), Case 2 is the simulation without gravity (black line), and Case 3 is for a constant density with gravity (cyan line). Regardless of whether the gravity is included in simulations, these three lines lead to similar expansion times. It indicates that the average initial density in which the H II region has expanded is one of the important parameters

for estimating expansion time. Once quenching by gravity has been overruled, the expansion is no longer strongly affected by gravity. In the details, however, the configuration with constant density and gravity underestimates the expansion time mainly in the central parts where the density should be much higher than what is estimated.

For the northern H II region, expansion simulated in a decreasing envelope without gravity gives a minimum expansion time of 355 kyr. Expansion simulated with gravity in a decreasing-density envelope with the highest possible central density gives a maximum time of 370 kyr. These values define a very narrow interval for the expansion time, if extrapolation of the observed envelope towards the interior is valid. Taking the observational uncertainties into account, including those concerning the small scales structure, we conclude that the expansion time of the northern H II region should be 350+/−50 kyr.

Even more strikingly, for the eastern H II region, we do not need to increase the default central core radius (0.005 pc), and the time expansion calculated with gravity (24 kyr) is almost identical to the time obtained without gravity (23 kyr). This shows again that gravity could delay the start of expansion, but has very small influence on expansion time. This effect is more pronounced in a low-density medium.

4.2.4. Ionisation age and expansion time

Tracing the expansion of H II regions with gravity and in a decreasing-density envelope extrapolated from the one observed at large scales would require complex 2D or even 3D configurations, at least on small scales. On large scales, in a decreasing-density envelope with a power law index $q \gtrsim 1$, once gravity has been overcome by turbulence and expansion occurs, the gravitational pressure decreases faster than the turbulent pressure, and its influence becomes negligible (Tremblin et al. 2014a, Sect. 5.1, Eq. (12)). Accretion within a rotating envelope can create a lower density zone where infall is driven from the envelope onto a disk or torus (see Tobin et al. 2008, Fig. 10; Hosokawa et al. 2010, Fig. 1; Ohashi et al. 2014, Fig. 5). The decreased density near the ionising objet reduces the influence of gravity. It should result in a reduction of the expansion time and decrease in re-collapse probability. Outflow lobes also modify the density structure and the geometry of the envelope (outflow cavity) and thus influence the expansion time. Infalling gas from the envelope itself locally increases the density and reduces the expansion speed or impedes it in a disk, torus, or funnel. All these effects, along with sporadic accretion (Peters et al. 2010a; Duarte-Cabral et al. 2013; De Pree et al. 2014), increase the expansion time uncertainty. A definitive measurement of the ionisation age would thus require a detailed modelling based on better constraints of physical parameters, at least on small scales. Unfortunately, the observational constraints of high-mass protostellar envelope on small scales (<0.05 pc) are still largely missing. This 3D small-scale asymmetric geometry could also shorten the quenching time, which needs to be added to the expansion time to determine the age of H II regions and their ionising stars. On the other hand, confinement by external pressure could also occur at the end of expansion and thus lengthen the ionisation age. Expansion times depend on the initial conditions on small scales and especially ionisation age if the quenching and confinement times are taken into account. However, the order of magnitude of the expansion times determined from simulations seems to converge (see Table 4).

The simulations performed with or without gravity for the eastern and northern H II regions expanding in low-density

envelopes provide expansion times of $25 \pm 5 \times 10^3$ yr and $350 \pm 50 \times 10^3$ yr. For the central UC and western compact H II regions, we estimated upper and lower limits for the expansion time. Lower limits correspond to simulations in a decreasing-density envelope without gravity (Table 4, Col. 6). Upper limits are given by simulations with gravity in an envelope with the highest constant density (Table 4, Col. 8) avoiding quenching or re-collapse and allowing the observed size to be reached. The ranges of time values obtained, $90-150 \pm 50 \times 10^3$ yr, are consistent with a mean expansion time of 1×10^5 yr. The expansion time of the central UCH II region, 9×10^4 yr, agrees with the duration of the warm phase in dedicated chemical models (10^4–a few 10^5 yr, Treviño-Morales et al. 2014). The chemical model requires a chemistry out of equilibrium and imply a warm phase duration of less than 10^6 yr.

Despite the dependence on unknown small scale geometry, expansion times adopted for the dense western compact and central UCH II regions are equal to within a factor two, converging to $\sim 1-1.5 \times 10^5$ yr (Table 4, Col. 10). They agree with the statistical estimate of the age of C and UCH II regions ($\sim 10^5$ yr, Wood & Churchwell 1989b) and are ten times longer than the rough dynamical time ($\sim 10^4$ yr) estimated from the initial ionised gas velocity. As already stressed by Urquhart et al. (2013), the order of magnitude of these ages, $3-6 \times 10^5$ yr, has recently been confirmed by new statistical lifetimes ($\sim 3 \times 10^5$ yr, Mottram et al. 2011) and supported by a Galactic population synthesis analysis ($2-4 \times 10^5$ yr, Davies et al. 2011). The so-called lifetime problem (Wood & Churchwell 1989b; Churchwell 2002; Peters et al. 2010b) is simply solved here by taking an expansion velocity equal to the sound speed in ionised gas (c_s) only at the beginning. Indeed, in a slowly decreasing-density envelope ($q < 1.5$) expansion speed is rapidly damped and even stopped if confinement by external turbulent pressure occurs (Raga et al. 2012).

4.3. Suitable approximations for expansion time estimation

As already mentioned in the previous section, gravity does not itself strongly affect the expansion time, but a delay of expansion can occur at the beginning. Similarly, Keto (2007) differentiates the dynamic behaviour of HC and UCH II regions, which are gravitationally dominated, from that of larger compact and extended H II regions, which are thermally dominated. As a matter of fact, in the low-density conditions of the northern and eastern regions, simulations with or without gravity give similar expansion times (see Table 4, Cols. 6 and 9). In the high-density condition of the central and western regions, the upper limit of expansion times calculated with gravity (Table 4, Col. 8), even with a rough constant density estimation, are only twice longer than expansion times obtained without gravity (Table 4, Col. 6).

Even if the average initial densities ($\langle \rho_{initial} \rangle$, Table 4, Col. 2) are only roughly estimated, expansion times of the various analytical calculations and simulations agree (Table 4, Cols. 3, 5, and 6). The agreement is better for the small (C and UC) H II regions, for which the average initial density is more representative of the overall past density conditions. Analytical calculations without gravity using an extrapolation of the observed density envelope give a good time estimate at least for H II regions of small sizes. For the more extended northern H II region, the evaluation made of the average envelope density on small scales is more questionable since the remaining envelope has much lower density than the one at the beginning of expansion. Calculations using more realistically extrapolated density profiles should be preferred, or other evaluation using the pressure equilibrium and third Larson law (Tremblin et al. 2014a) could be made.

We conclude that:

- Gravity induces quenching, which adds a delay before the H II region expands, but when it expands, the influence of gravity becomes marginal.
- Envelope density profiles could be used to estimate a minimum expansion time from analytical calculations without gravity, and if density is not too high, it gives a realistic value.
- The mean initial density is a good estimator of the matter density surrounding the massive protostar in early stages and is later collected in the shell by the H II region expansion. It could be used to estimate expansion times if density profiles are not well defined. In any case, it is better suited to describe the intial density condition of ionisation expansion than the surrounding cloud density characterising the external medium.

All realistic time expansion estimates done in this paper converge around $\sim 1 \times 10^5$ yr for the two dense (UC central and compact western) H II regions, $\sim 2.5 \times 10^4$ yr for the compact eastern H II region, and $\sim 3.5 \times 10^5$ yr for the extended northern H II region.

5. History of the formation of the B-type stars powering H II regions in Mon R2

In Sect. 5.1, we discuss the global infall of the Mon R2 cloud. In Sect. 5.2, we analyse the two-slope profiles in the framework of the inside-out collapse of envelopes and estimate protostellar infall ages. In Sect. 5.3, we compare the infall and ionisation ages and propose a full history of massive star formation in the Mon R2 cloud.

5.1. Cloud global infall

The density structure and infall kinematics discussed here are probably dominated by the most massive object clearly identified in Fig. 2b. The envelope profile defined above (see Sect. 3.5) and their corresponding values given in Table 3 have been used in Eq. (A.2) to estimate a mass of $\sim 3500\ M_\odot$ in a 2.5 pc radius for the central UCH II region. This region exhibits a steeper density gradient in its outer envelope, with $q_{out} \simeq -2.5$, also illustrated by the cloud structure studied with probability density function (Schneider et al. 2015; Rayner et al., in prep.). It suggests compression by external forces, as shown in numerical simulations of Hennebelle et al. (2003) and outlined in Appendix A. This compressive process could be associated with stellar winds and ionisation shocks of nearby stars such as those observed in the M 16 massive YSO (young stellar object) by Tremblin et al. (2014b) or with globally infalling gas driven by the dynamic formation of Mon R2 cloud through force fall. Such infalling motions have in fact been observed in CO by Loren (1977), and clumps with similar masses generally exhibit active global infall. This is the case of SDC335, which has a mass of $\sim 5500\ M_\odot$ in 2.5 pc (Peretto et al. 2013) and contains a protostellar object of similar type B1 (Avison et al. 2015), as well as of DR21, Clump-14 (DR21-south, $\sim 4900\ M_\odot$), and Clump-16 (DR21-north, $\sim 3350\ M_\odot$) (Schneider et al. 2010a), all of which show supersonic infall ($V = 0.5-0.7$ km s^{-1}). Moreover, the hourglass morphology of the magnetic field is thought to be a signature of global infall (Carpenter & Hodapp 2008), and Koch et al. (2014) suggest that Mon R2 is a super critical, quickly collapsing cloud. The expected infall velocity gradient, as observed

in SDC13 (Peretto et al. 2014), seems to be a crucial ingredient for generating the filament crossing (Dobashi et al. 2014) characteristic of all the regions mentioned here and commonly observed in many places.

5.2. Time elapsed since the beginning of the protostellar infall

The outer envelope of the two compact eastern and western H II regions display a column density index of $p_{out} \simeq -1 \pm 0.2$, which corresponds to a $\rho(r) \propto r^{-2}$ density law. It recalls the density distribution of the singular isothermal sphere (SIS, Shu 1977) and that of the cloud structures quasi-statically forming clumps in numerical simulations with or without turbulence and magnetic field (e.g. Li & Shu 1996). A similar density distribution is in fact obtained for clumps forming from subsonic infall (Dalba & Stahler 2012) or supersonic flows (Gong & Ostriker 2009). This is also reminiscent of the density profiles found for low-mass and high-mass protostellar envelopes in early stages (Tsitali et al. 2013), which has been known for a long time (e.g. Motte & André 2001; Beuther et al. 2002). Numerous pre-main sequence phase YSOs are found in the Mon R2 cloud, suggesting that a group or cluster of protostars has most probably formed within the same area of these four separate envelopes of $\sim 2.5-3$ pc radius each.

The transition radius between the inner and outer envelopes, R_{Infall}, could be used to locate the front of the infall expansion wave associated with the protostellar collapse. Indeed, in the case of an inside-out collapse developing into a static envelope with a SIS density structure, the envelope matter is free-falling as soon as the infall front wave travelling outwards reaches its location (e.g. Shu 1977). Interestingly, the density profile measured for the inner envelope surrounding H II regions is close to that of free-falling material, $\rho(r) \propto r^{-1.5}$ (see Table 3). The transition radii would correspond to late stages of the protostellar collapse since they are rather large compared to typical protostellar envelopes: $R_{Infall} \sim 0.3, 0.5, 0.9, 2$ pc versus $R_{prot} \sim 0.03-0.1$ pc (e.g. Motte & André 2001). This free-falling envelope material may not be able to reach the stars but may pile up at the periphery of the H II regions, located at $R_{H II}$.

We assumed below that the infall front wave initiated at the time of the protostellar embryo formation and propagating outwards from the centre can be approximated by R_{Infall}. The latter was measured to be 0.3, 0.5, and 0.9 pc for the central, western, and eastern ultra-compact and compact H II region envelopes (see Table 3). We used an infall front-wave velocity equal to the isothermal sound speed, $a_s = c_s = \sqrt{k\,T/\mu\,m_H} \simeq 0.2$ km s^{-1}, calculated for $T = 13.5$ K, which is the mean cloud temperature in Mon R2. We then dated the beginning of the protostellar infall using the following equation:

$$t_{Infall} = \frac{R_{Infall}}{c_s} \simeq 4.9 \times 10^6 \text{ yr} \times \frac{R_{Infall}}{1\,\text{pc}} \times \left(\frac{c_s}{0.2\,\text{km s}^{-1}}\right)^{-1}. \quad (11)$$

It dates back to a few million years ago for the three compact and ultra-compact H II regions with $t_{Infall} \simeq 1.5 \times 10^6$ yr for the UCH II and $t_{Infall} \sim 2.5-4.5 \times 10^6$ yr for the eastern and western H II regions. The more developed northern H II region has an envelope that could be fully free-falling up to a radius reaching the background density (see Table 3). With a value of $R_{Infall} > 2$ pc, our calculation leads to a minimum infall age of $t_{Infall} > 10^7$ yr. These ages perhaps seem too long, but they are approximate values since a more complex density, temperature, and kinematic structure is to be expected for a non-isothermal envelope that is

already globally collapsing at the time of the creation of the first protostellar embryo.

Moreover, the static SIS initial conditions are probably far from realistic, particularly for clouds forming high-mass stars, which are known to be dynamical entities (Schneider et al. 2010a; Peretto et al. 2013). Some models examined the protostellar collapse in an infalling cloud (Larson 1969; Penston 1969; Gong & Ostriker 2009; Keto et al. 2015). The initial inflow speed before protostellar collapse indeed modifies directly or indirectly the rarefaction wave speed, even in subsonic mode (Dalba & Stahler 2012). In the case of supersonic flows, the speed increases by a factor 2 to 3 (Gong & Ostriker 2009, see their Sect. 4.2), dividing the calculated infall time by the same factor. Supersonic inflows driven by the cloud's global collapse, is probable for the central UCH II region. It is less certain but still plausible for the other H II regions, which are within the same infalling cloud but excentred from the infall centre.

Infall times are listed in Col. 6 of Table 3. The range of values illustrates systematics and errors to statistical uncertainties. All in all, it gives the following infall times: $\sim 1. \pm .7 \times 10^6$ yr for the central UCH II region, $\sim 1.5 \pm 1. \times 10^6$ yr for the western CH II region, and $\sim 3. \pm 1.5 \times 10^6$ yr for the eastern CH II region. Deducing the ionisation expansion time estimated in Sect. 4 from this infall time provides a measure of the time a protostar needs to reach the high-mass regime associated with the emission of ionising UV photons and an eventual ionisation delay due to quenching or swelling (Hoare & Franco 2007).

5.3. Age comparison and history of OB star formation in Mon R2

For the dense compact and ultra-compact (western and central) H II regions, infall ages derived in Sect. 5.2: are about ten times greater than the ionisation expansion time $t_{infall} \sim 1-2 \times 10^6$ yr versus $t_{ionisation} \sim 1-2 \times 10^5$ yr. As for the eastern compact H II region, the infall time is 100 times longer than the ionisation expansion time: $t_{infall} \sim 3 \times 10^6$ yr versus $t_{ionisation} \sim 25 \times 10^3$ yr. The infall age of the northern extended H II region is unknown with a lower limit of $t_{infall} > 14 \times 10^6$ yr, which is ~ 30 times more than the ionisation expansion time of $t_{ionisation} \sim 5 \times 10^5$ yr. Even if uncertain, the order of magnitude of these values is probably realistic since the stellar ages of the B-type star association observed in Mon R2 is $\sim 1-6 \times 10^6$ yr (Herbst & Racine 1976; Carpenter et al. 1997), in agreement with the computed infall ages of the compact and ultra-compact H II region envelopes.

Subtracting a mean protostellar lifetime of 3×10^5 yr (Duarte-Cabral et al. 2013; see also Schisano et al. 2014, and references therein) from the infall time measured for the central UCH II region, 1×10^6 yr suggests that ionisation started 7×10^5 yr ago. With an ionisation expansion time of $\sim 1 \times 10^5$ yr, the quenching delay time could be $\sim 6 \pm 5 \times 10^5$ yr. The typical protostellar lifetime adopted here agrees with the one obtained for the cold phase of Mon R2 in chemical models (10^5-10^6 yr, Treviño-Morales et al. 2014), corresponding to collapse (Esplugues et al. 2014). Similar considerations for western (and eastern) CH II region give a quenching delay time of $\sim 9 \pm 6 \times 10^5$ yr (resp. $\sim 2 \pm 1 \times 10^6$ yr). These variations could be interpreted as an increase in the quenching time with increasing spectral type from B0 to B2.5, and thus decreasing number of ionising photons N_{Lyc}. However, given the large uncertainties of each of these estimates, a constant value around 10^6 yr cannot be ruled out.

Besides that, the derived infall ages span an order-of-magnitude difference, possibly indicating progressive star

formation in the Mon R2 cloud. None of the ionisation fronts and none of the infall rarefaction wave arising from the three H II regions located ~1–2 pc from the UCH II region could, however, explain the compression of the UCH II envelope. There is thus no clear evidence that star formation in the Mon R2 cloud could have been triggered by older local populations of stars. Any observed age gradient could only be related to sequential star formation triggered by an external agent.

6. Conclusions

We have presented a study of the Mon R2 molecular cloud based on dust column density and temperature maps built from *Herschel*/HOBYS observations and dedicated simuations. Our main findings can be summarised as follows:

1) The MonR2 molecular cloud is dominated by gas associated with the central UCH II region. The latter is located at the crossing of three major filaments, while three other H II regions develop in their surroundings. The spectral type of ionising stars as estimated from 21cm fluxes are in very good agreement with those obtained from visual spectroscopy. They all are early B-type stars.

2) The size of ionised regions is estimated by the heating of big grains (Fig. 2a) and small grains excitation through their $70\,\mu m$ flux (Fig. 5), in the close surrounding of H II regions, probably within the PDR. It ranges from ~0.1 pc for compact and UCH II regions to ~0.8 pc for the most classical extended H II region.

3) The H II regions are surrounded by large and rather dense neutral gas envelopes ($R_{\rm env} \sim$ 2–3 pc, $\rho_{\rm env}^{\rm max} \sim 3 \times 10^2$–$5 \times 10^5$ cm^{-3}). At radii from ~0.1 pc to a few parsecs, the envelope surrounding H II regions cannot be considered to have a constant density. Temperature gradients are also observed in the neutral gas envelope surrounding the four regions.

4) In spite of the quite advanced stage of evolution of the four massive ionising stars studied here, the density of the envelope surrounding them keep the imprint of earlier phases of the gravitational collapse. The density structure is similar to those expected for individual protostellar objects. For the first time the power law slope of the density profile is constrained accurately enough to distinguish between inner layers in free fall ($\rho \propto r^{-w}$ with $w \leqslant 1.5$) and external parts that could correspond to an equilibrium SIS configuration ($\rho \propto r^{-2}$).

5) We interpret the steep density profile of the central UCH II region ($\rho \propto r^{-2.5}$) as due to an external pressure certainly associated with the observed global collapse, which can be called a forced fall.

6) The transition radius between $\rho \propto r^{-1.5}$ (or r^{-w} with $w \leqslant 1.5$) and r^{-2} (or r^{-w} with $w \geqslant 2$) laws should locate the free-fall rarefaction wave. Assuming it expands at one to three times the sound speed, we estimate the time since the infall began. An infall age around a few million years for these H II regions is consistent with current high-mass star formation scenarios.

7) The density profiles obtained here allow us to determine the initial conditions of ionisation and its expansion. Dedicated 1D simulations show that the envelope density presently observed on a large scale would induce a complete quenching of the ionisation expansion. A more complex geometry on a small scale and a dynamic scenario are required to explain the present H II region development.

8) The ionisation expansion time deduced here from analytical calculations and dedicated simulations agree with statistical ages of the corresponding H II region. The compact and UCH II region expansion time is 1–2×10^5 yr.

Stellar formation in MonR2 seems to be an on-going process that started at least ~1–6×10^6 yr ago. Large scale feedback, such as the global infall of the cloud complex, certainly play an important role, but no clear evidence of locally triggered star formation has been found.

References

Anderson, L. D., Zavagno, A., Deharveng, L., et al. 2012, A&A, 542, A10
Anderson, L. D., Deharveng, L., Zavagno, A., et al. 2015, ApJ, 800, 101
Andre, P., Ward-Thompson, D., & Barsony, M. 2000, Protostars and Planets IV, 59
Arthur, S. J., Henney, W. J., Mellema, G., de Colle, F., & Vázquez-Semadeni, E. 2011, MNRAS, 414, 1747
Aspin, C., & Walther, D. M. 1990, A&A, 235, 387
Avison, A., Peretto, N., Fuller, G. A., et al. 2015, A&A, 577, A30
Bacmann, A., André, P., Puget, J.-L., et al. 2000, A&A, 361, 555
Bernard, J.-P., Paradis, D., Marshall, D. J., et al. 2010, A&A, 518, L88
Beuther, H., Schilke, P., Menten, K. M., et al. 2002, ApJ, 566, 945
Bohlin, R. C., Savage, B. D., & Drake, J. F. 1978, ApJ, 224, 132
Bonnor, W. B. 1956, MNRAS, 116, 351
Carmona, A., Pinte, C., Thi, W. F., et al. 2014, A&A, 567, A51
Carpenter, J. M., & Hodapp, K. W. 2008, The Monoceros R2 Molecular Cloud (Reipurth, B.), 899
Carpenter, J. M., Meyer, M. R., Dougados, C., Strom, S. E., & Hillenbrand, L. A. 1997, AJ, 114, 198
Chini, R., Hoffmeister, V. H., Nielbock, M., et al. 2006, ApJ, 645, L61
Churchwell, E. 2002, ARA&A, 40, 27
Churchwell, E., Watson, D. F., Povich, M. S., et al. 2007, ApJ, 670, 428
Compiègne, M., Verstraete, L., Jones, A., et al. 2011, A&A, 525, A103
Condon, J. J., Cotton, W. D., Greisen, E. W., et al. 1998, AJ, 115, 1693
Dalba, P. A., & Stahler, S. W. 2012, MNRAS, 425, 1591
Davies, B., Hoare, M. G., Lumsden, S. L., et al. 2011, MNRAS, 416, 972
de Gregorio-Monsalvo, I., Ménard, F., Dent, W., et al. 2013, A&A, 557, A133
De Pree, C. G., Peters, T., Mac Low, M.-M., et al. 2014, ApJ, 781, L36
Deharveng, L., Zavagno, A., & Caplan, J. 2005, A&A, 433, 565
Deharveng, L., Zavagno, A., Anderson, L. D., et al. 2012, A&A, 546, A74
Dobashi, K., Matsumoto, T., Shimoikura, T., et al. 2014, ApJ, 797, 58
Downes, D., Winnberg, A., Goss, W. M., & Johansson, L. E. B. 1975, A&A, 44, 243
Duarte-Cabral, A., Bontemps, S., Motte, F., et al. 2013, A&A, 558, A125
Dyson, J. E., & Williams, D. A. 1980, Physics of the interstellar medium (New York: Halsted Press), 204
Ebert, R. 1955, ZAp, 37, 217
Elmegreen, B. G., & Lada, C. J. 1977, ApJ, 214, 725

Esplugues, G. B., Viti, S., Goicoechea, J. R., & Cernicharo, J. 2014, A&A, 567, A95

Franco, J., Tenorio-Tagle, G., & Bodenheimer, P. 1990, ApJ, 349, 126

Fuente, A., Berné, O., Cernicharo, J., et al. 2010, A&A, 521, L23

Galliano, F., Hony, S., Bernard, J.-P., et al. 2011, A&A, 536, A88

Giannakopoulou, J., Mitchell, G. F., Hasegawa, T. I., Matthews, H. E., & Maillard, J.-P. 1997, ApJ, 487, 346

Gong, H., & Ostriker, E. C. 2009, ApJ, 699, 230

Gong, H., & Ostriker, E. C. 2013, ApJS, 204, 8

González, M., Audit, E., & Huynh, P. 2007, A&A, 464, 429

Griffin, M. J., Abergel, A., Abreu, A., et al. 2010, A&A, 518, L3

Gutermuth, R. A., Pipher, J. L., Megeath, S. T., et al. 2011, ApJ, 739, 84

Harsono, D., Jørgensen, J. K., van Dishoeck, E. F., et al. 2014, A&A, 562, A77

Hennebelle, P., Whitworth, A. P., Gladwin, P. P., & André, P. 2003, MNRAS, 340, 870

Henning, T., Chini, R., & Pfau, W. 1992, A&A, 263, 285

Herbst, W., & Racine, R. 1976, AJ, 81, 840

Hildebrand, R. H. 1983, Quant. J. Roy. Astron. Soc., 24, 267

Hill, T., Pinte, C., Minier, V., Burton, M. G., & Cunningham, M. R. 2009, MNRAS, 392, 768

Hill, T., Motte, F., Didelon, P., et al. 2011, A&A, 533, A94

Hill, T., Motte, F., Didelon, P., et al. 2012, A&A, 542, A114

Hindson, L., Thompson, M. A., Urquhart, J. S., et al. 2012, MNRAS, 421, 3418

Hoare, M. G., & Franco, J. 2007, ArXiv eprints [arXiv:0711.4912H]

Hosokawa, T., & Inutsuka, S.-I. 2005, ApJ, 623, 917

Hosokawa, T., & Inutsuka, S.-I. 2006, ApJ, 646, 240

Hosokawa, T., Yorke, H. W., & Omukai, K. 2010, ApJ, 721, 478

Immer, K., Cyganowski, C., Reid, M. J., & Menten, K. M. 2014, A&A, 563, A39

Jaffe, D. T., Zhu, Q., Lacy, J. H., & Richter, M. 2003, ApJ, 596, 1053

Jeffers, S. V., Min, M., Canovas, H., Rodenhuis, M., & Keller, C. U. 2014, A&A, 561, A23

Ji, W.-G., Zhou, J.-J., Esimbek, J., et al. 2012, A&A, 544, A39

Keto, E. 2007, ApJ, 666, 976

Keto, E., Caselli, P., & Rawlings, J. 2015, MNRAS, 446, 3731

Koch, P. M., Tang, Y.-W., Ho, P. T. P., et al. 2014, ApJ, 797, 99

Kurtz, S., Churchwell, E., & Wood, D. O. S. 1994, ApJS, 91, 659

Larson, R. B. 1969, MNRAS, 145, 271

Li, Z.-Y., & Shu, F. H. 1996, ApJ, 472, 211

Loren, R. B. 1977, ApJ, 215, 129

Maret, S., Belloche, A., Maury, A. J., et al. 2014, A&A, 563, L1

Martín-Hernández, N. L., Vermeij, R., & van der Hulst, J. M. 2005, A&A, 433, 205

Massi, M., Felli, M., & Simon, M. 1985, A&A, 152, 387

Meyers-Rice, B. A., & Lada, C. J. 1991, ApJ, 368, 445

Minier, V., Tremblin, P., Hill, T., et al. 2013, A&A, 550, A50

Motte, F., & André, P. 2001, A&A, 365, 440

Motte, F., Zavagno, A., Bontemps, S., et al. 2010, A&A, 518, L77

Motte, F., Bontemps, S., Hennemann, M., et al. 2012, in SF2A-2012: Proc. Annual meeting of the French Society of Astronomy and Astrophysics, eds. S. Boissier, P. de Laverny, N. Nardetto, et al., 45

Mottram, J. C., Hoare, M. G., Davies, B., et al. 2011, ApJ, 730, L33

Mueller, K. E., Shirley, Y. L., Evans, II, N. J., & Jacobson, H. R. 2002, ApJS, 143, 469

Nguyen-Luong, Q., Motte, F., Carlhoff, P., et al. 2013, ApJ, 775, 88

Nielbock, M., Launhardt, R., Steinacker, J., et al. 2012, A&A, 547, A11

Ochsenbein, F., Bauer, P., & Marcout, J. 2000, A&AS, 143, 23

Ohashi, N., Saigo, K., Aso, Y., et al. 2014, ApJ, 796, 131

Panagia, N. 1973, AJ, 78, 929

Penston, M. V. 1969, MNRAS, 144, 425

Peretto, N., Fuller, G. A., Duarte-Cabral, A., et al. 2013, A&A, 555, A112

Peretto, N., Fuller, G. A., André, P., et al. 2014, A&A, 561, A83

Peters, T., Banerjee, R., Klessen, R. S., et al. 2010a, ApJ, 711, 1017

Peters, T., Mac Low, M.-M., Banerjee, R., Klessen, R. S., & Dullemond, C. P. 2010b, ApJ, 719, 831

Pilbratt, G. L., Riedinger, J. R., Passvogel, T., et al. 2010, A&A, 518, L1

Pilleri, P., Fuente, A., Cernicharo, J., et al. 2012, A&A, 544, A110

Pilleri, P., Treviño-Morales, S., Fuente, A., et al. 2013, A&A, 554, A87

Pilleri, P., Fuente, A., Gerin, M., et al. 2014, A&A, 561, A69

Poglitsch, A., Waelkens, C., Geis, N., et al. 2010, A&A, 518, L2

Quireza, C., Rood, R. T., Bania, T. M., Balser, D. S., & Maciel, W. J. 2006, ApJ, 653, 1226

Racine, R. 1968, AJ, 73, 233

Raga, A. C., Cantó, J., & Rodríguez, L. F. 2012, MNRAS, 419, L39

Richardson, K. J., White, G. J., Monteiro, T. S., & Hayashi, S. S. 1988, A&A, 198, 237

Roccatagliata, V., Preibisch, T., Ratzka, T., & Gaczkowski, B. 2013, A&A, 554, A6

Roussel, H. 2013, PASP, 125, 1126

Schisano, E., Rygl, K. L. J., Molinari, S., et al. 2014, ApJ, 791, 27

Schneider, N., Csengeri, T., Bontemps, S., et al. 2010a, A&A, 520, A49

Schneider, N., Motte, F., Bontemps, S., et al. 2010b, A&A, 518, L83

Schneider, N., Bontemps, S., Simon, R., et al. 2011, A&A, 529, A1

Schneider, N., Bontemps, S., Girichidis, P., et al. 2015, ArXiv e-prints [arXiv:1507.08869]

Shu, F. H. 1977, ApJ, 214, 488

Shu, F. H., Lizano, S., Galli, D., Cantó, J., & Laughlin, G. 2002, ApJ, 580, 969

Spitzer, L. 1978, Physical processes in the interstellar medium (New York: Wiley-Interscience)

Strömgren, B. 1939, ApJ, 89, 526

Strömgren, B. 1948, ApJ, 108, 242

Tang, X. D., Esimbek, J., Zhou, J. J., et al. 2013, A&A, 551, A28

Taylor, M. B. 2005, in Astronomical Data Analysis Software and Systems XIV, eds. P. Shopbell, M. Britton, & R. Ebert, ASP Conf. Ser., 347, 29

Thronson, Jr., H. A., Gatley, I., Harvey, P. M., Sellgren, K., & Werner, M. W. 1980, ApJ, 237, 66

Tobin, J. J., Hartmann, L., Calvet, N., & D'Alessio, P. 2008, ApJ, 679, 1364

Tremblin, P., Audit, E., Minier, V., Schmidt, W., & Schneider, N. 2012a, A&A, 546, A33

Tremblin, P., Audit, E., Minier, V., & Schneider, N. 2012b, A&A, 538, A31

Tremblin, P., Minier, V., Schneider, N., et al. 2013, A&A, 560, A19

Tremblin, P., Anderson, L. D., Didelon, P., et al. 2014a, A&A, 568, A4

Tremblin, P., Schneider, N., Minier, V., et al. 2014b, A&A, 564, A106

Treviño-Morales, S. P., Pilleri, P., Fuente, A., et al. 2014, A&A, 569, A19

Tsitali, A. E., Belloche, A., Commerçon, B., & Menten, K. M. 2013, A&A, 557, A98

Urquhart, J. S., Thompson, M. A., Moore, T. J. T., et al. 2013, MNRAS, 435, 400

van den Bergh, S. 1966, AJ, 71, 990

Walmsley, M. 1995, Rev. Mex. Astron. Astrofis., 27, 137

Whalen, D., & Norman, M. L. 2006, ApJS, 162, 281

Wilson, B. A., Dame, T. M., Masheder, M. R. W., & Thaddeus, P. 2005, A&A, 430, 523

Wood, D. O. S., & Churchwell, E. 1989a, ApJ, 340, 265

Wood, D. O. S., & Churchwell, E. 1989b, ApJS, 69, 831

Xie, T., & Goldsmith, P. F. 1994, ApJ, 430, 252

Yun, J. L., & Clemens, D. P. 1991, ApJ, 381, 474

Zavagno, A., Russeil, D., Motte, F., et al. 2010, A&A, 518, L81

Zhu, Q.-F., Lacy, J. H., Jaffe, D. T., Richter, M. J., & Greathouse, T. K. 2005, ApJ, 631, 381

Zhu, Q.-F., Lacy, J. H., Jaffe, D. T., Richter, M. J., & Greathouse, T. K. 2008, ApJS, 177, 584

[1] Laboratoire AIM, CEA/IRFU CNRS/INSU Université Paris Diderot, CEA-Saclay, 91191 Gif-sur-Yvette Cedex, France
e-mail: pierre.didelon@cea.fr

[2] Astrophysics Group, University of Exeter, EX4 4QL Exeter, UK

[3] Maison de la Simulation, CEA-CNRS-INRIA-UPS-UVSQ, USR 3441, Centre d'étude de Saclay, 91191 Gif-Sur-Yvette, France

[4] Joint ALMA Observatory, 3107 Alonso de Cordova, Vitacura, Santiago, Chile

[5] Universität Heidelberg, Zentrum für Astronomie, Institut für Theoretische Astrophysik, Albert-Ueberle-Str. 2, 69120 Heidelberg, Germany

[6] Department of Physics and Astronomy, West Virginia University, Morgantown, WV 26506, USA

[7] Also Adjunct Astronomer at the National Radio Astronomy Observatory, PO Box 2, Green Bank, WV 24944, USA

[8] Université de Bordeaux, OASU, Bordeaux, France

[9] Cardiff University, Wales Cardiff CF103 XQ, UK

[10] European Space Research and Technology Centre (ESA-ESTEC), Keplerlaan 1, PO Box 299, 2200 AG Noordwijk, The Netherlands

[11] Cerro Calan, Observatorio Astronmico Nacional, Camino el Observatorio, 1515 Las Condes, Chile

[12] Laboratoire d'Astrophysique de Marseille, CNRS/INSU–Université de Provence, 13388 Marseille Cedex 13, France

[13] Queen Mary + Westf. College, Dept. of Physics, London E1 4NS, UK

[14] CESR, 31028 Toulouse, France

[15] INAF–Istituto di Astrofisica e Planetologia Spaziali, via Fosso del Cavaliere 100, 00133 Rome, Italy

[16] National Research Council of Canada, Herzberg Institute of Astrophysics, 5071 West Saanich Rd., Victoria, BC, V9E 2E7, Canada

[17] University of Victoria, Department of Physics and Astronomy, PO Box 3055, STN CSC, Victoria, BC, V8W 3P6, Canada

[18] National Astronomical Observatory of Japan, Chile Observatory, 2-21-1 Osawa, Mitaka, 181-8588 Tokyo, Japan

[19] Université de Toulouse, UPS-OMP, IRAP; CNRS, IRAP, 9 avenue colonel Roche, BP 44346, 31028 Toulouse Cedex 4, France

[20] Jeremiah Horrocks Institute, University of Central Lancashire, Preston, PR1 2HE Lancashire, UK

[21] Department of Physical sciences, The Open University, Milton Keynes MK7 6AA, UK

[22] RALspace, The Rutherford Appleton Laboratory, Chilton, Didcot OX110QX, UK

Appendix A: H ɪɪ region expansion in an envelope of decreasing density with power law profile

A.1. Mass and average density from a decreasing power law density profile

When considering a decreasing density distribution described by a power law with an index q, $\rho(r) = \rho_1 r^{-q}$, the mass included within a radius R is given by

$$M(R) = \int_0^R \rho_1 r^{-q} 4\pi r^2 \mathrm{d}r = 4\pi\rho_1 \int_0^R r^{2-q}\mathrm{d}r. \tag{A.1}$$

As far as $q < 3$, it gives

$$M(R) = 4\pi\rho_1 \frac{R^{3-q}}{3-q}, \tag{A.2}$$

or in numerical terms

$$M(R) = 0.76646\left(\rho_1\,\mathrm{cm}^{-3}\right)\frac{(R\,\mathrm{pc})^{3-q}}{3-q}M_\odot. \tag{A.3}$$

The mean density in the sphere of radius R is then given by

$$\langle\rho(R)\rangle = M(R)\frac{3}{4\pi R^3} = \left(\frac{3}{3-q}\right)\rho_1 R^{-q} = \left(\frac{3}{3-q}\right)\rho(R), \tag{A.4}$$

and for a gradient typical of infall, $q = 1.5$, it gives

$$\langle\rho(R)\rangle = 2\rho_1 R^{-3/2} = 2\rho(R).$$

A.2. Ionisation expansion in a decreasing power law density profile

We consider here a decreasing density distribution with a power law of index q and a central core of constant density to avoid singularity at the origin and mimic a core envelope using the same definition as in Eq. (8):

$$\rho = \begin{cases} \rho_c & \text{for} & r \le r_c \\ \rho_1 \times r^{-q} & \text{for} & r > r_c \\ & \text{with } \rho_c = \rho_1 \times r_c^{-q}. \end{cases} \tag{A.5}$$

Considering the density, ρ_i, and the speed, c_i, in the ionised medium, the speed of the shell V, from the Rankine-Hugoniot conditions (Eq. (B.5), Minier et al. 2013) we get

$$\rho_i c_i^2 \approx \rho(r) V^2 \tag{A.6}$$

using the density profile of (Eqs. (8)/(A.5)), it transforms into

$$\rho_i c_i^2 \approx \rho_1 \times r^{-q} V^2 \approx \rho_c \times \left(\frac{r}{r_c}\right)^{-q} V^2. \tag{A.7}$$

Considering an initial Strömgren radius smaller than the core radius r_c, Eq. (6) and the photon conservation gives

$$\rho_c{}^2 R_{\mathrm{Str}}{}^3 = \rho_i{}^2 r^3 \Leftrightarrow \frac{\rho_c}{\rho_i} = \left(\frac{r}{R_{\mathrm{Str}}}\right)^{3/2}. \tag{A.8}$$

Equation (A.7) can then be written as

$$V \approx \left(\frac{r_c}{r}\right)^{-q/2}\left(\frac{R_{\mathrm{Str}}}{r}\right)^{3/4} c_i \approx r_c^{-q/2} R_{\mathrm{Str}}^{3/4} c_i \left(\frac{1}{r}\right)^{(3-2q)/4}. \tag{A.9}$$

Table B.1. Column density dependance to power law index of decreasing density envelope.

q	Integral $I(a)$ analytical	numerical	$\Sigma_1/1\,\mathrm{pc}$	ζ
1	$\ln\left(y + \sqrt{y^2 + a^2}\right)$	(1)	–	–
3/2	$2.6218/\sqrt{a}$	$2.6/\sqrt{a}$	$5.2\rho_1$	5.2
2	$1/a\,\arctan\left(y/a\right)$	$\pi/2a$	$\pi\rho_1$	π
5/2	$1.1985/\sqrt{a^3}$	$1.2/\sqrt{a^3}$	$2.4\rho_1$	2.4
3	$y/\left(a\sqrt{y^2 + a^2}\right)$	$1/a^2$	$2\rho_1$	2

Notes. (1) Analytical solution diverges at ∞. Integration can only be done on a spatialy limited size, and analytical values will depend on the outside radius R_{out}.

This equation can be integrated to give the radius of the shell, r_{shell}, as a function of time with t_c the time at which the shell reaches r_c:

$$r_{\mathrm{shell}} = r_c\left(1 + \frac{7-2q}{4}\frac{R_{\mathrm{Str}}^{3/4}}{r_c^{7/4}}c_i(t - t_c)\right)^{4/(7-2q)}. \tag{A.10}$$

Equation (A.9) taken at r_c allows defining the speed at this point,

$$V(r_c) = V_c \approx c_i\left(\frac{R_{\mathrm{Str}}}{r_c}\right)^{3/4}, \tag{A.11}$$

and can be introduced in Eq. (A.10)

$$r_{\mathrm{shell}} = r_c\left(1 + \frac{7-2q}{4}\frac{V_c}{r_c}(t - t_c)\right)^{4/(7-2q)}. \tag{A.12}$$

Appendix B: Column density line of sight calculation from an envelope of decreasing density with a power law profile

When considering a decreasing density distribution with a power law of index q:$\rho(r) = \rho_1 r^{-q}$, the column density as measured along the y axis at impact parameter a is given by

$$\Sigma(a) = 2\int_0^\infty \rho_1 r^{-q}\mathrm{d}y = 2\rho_1\int_0^\infty \left(\sqrt{a^2 + y^2}\right)^{-q}\mathrm{d}y \tag{B.1}$$

with $I(x) = \int_0^\infty \left(\sqrt{x^2 + y^2}\right)^{-q}\mathrm{d}y = \int_0^\infty \left(x^2 + y^2\right)^{-q/2}\mathrm{d}y$, the column density at impact parameter a is then given by

$$\Sigma(a) = 2\rho_1 I(a). \tag{B.2}$$

The analytical integration for integer values of q leads to well-known integrals already calculated by Yun & Clemens (1991). Half integers lead to elliptical integrals, and their tabulated values result in a polynomial expression of $I(a)$. The analytical and numerical values are given in Cols. 2 and 3 of Table B.1. Adopting a value of 1 pc for the impact parameter a, we can derive a relation between the column density and the density via $\Sigma_1(a = 1\,\mathrm{pc}) = 2\rho_1 I(a = 1\,\mathrm{pc})$. The relation of ρ_1 as a function of Σ_1 uses the conversion factor ζ corresponding to the appropriate q value and given in Col. 5 of Table B.1:

$$\rho_1 = \frac{\Sigma_1}{\zeta \times 1\,\mathrm{pc/cm}} = \frac{1000}{3.08 \times \zeta}\,\mathrm{cm}^{-3}\frac{\Sigma_1}{10^{21}\,\mathrm{cm}^{-2}}. \tag{B.3}$$

The dependence between ζ and q is given at the 5% error level by the following relation

$$\zeta = \frac{\pi}{(q-1)^{2/3}}. \tag{B.4}$$

Table C.1. Envelope density power law slope dependence on compression at two time step of protostellar stage.

ϕ	10	3	1	.3	.1
Time step 4: Class 0 start	–2.1	–2.1	–2.2	–1.9	–2.
Time step 5: Class I start	–1.5	–1.6	–1.65	–1.7	–1.8

Appendix C: Density gradient steepening by external compression, as seen in simulations

Hennebelle et al. (2003) have made numerical simulations to test the influence on density profiles of compression induced by additional external pressure. The compression is characterised (see their Eq. (12)) by a dimensionless factor (ϕ) that gives the number of sound-crossing times needed to double the external pressure. High ϕ values correspond to low compression, called subsonic and slow pression increase. Hennebelle et al. (2003) show radial density and velocity profile at five time steps. The three first ones correspond to prestellar phases, well represented by Bonnor-Ebert spheres (Bonnor 1956; Ebert 1955). The fourth step would correspond to the protostellar class 0 phase and the last one to the beginning of the class I phase (see Andre et al. 2000 for classes 0 and I definitions). For a supersonic compression ($\phi < 1$) during the prestellar phase, a density wave crosses the core profile towards the interior. For a sonic or subsonic compression ($\phi \geqslant 1$), the Bonnor-Ebert sphere like profile is smoothly distorted during prestellar phases leading to a single power law in protostellar phases.

We measured and give in Table C.1 the variation in the density profile power law index (q) as a function of the compression factor ϕ during the two time steps corresponding to the beginning and the end of Class 0 phase, (steps 4 and 5). During the Class 0 phase, the slope of the density profile does not depend on the compression and remains $q = -2$, the classical value expected for hydrostatic equilibrium. At the end of the Class 0 phase, the slope of the power law fitting the density profile is correlated to the compression given by the ϕ value (see Table C.1). It increases from 1.5, the classical value of a free-falling envelope, to 1.8 when ϕ varies from 10 (virtually no compression) to .1 (strongly supersonic compression). This 20% steepening of the density profile could be one effect that also occurs at a later stage and to larger radii as observed in the MonR2 central UCH II region, as advocated in Sect. 5.2.

Appendix D: H II region swept-up shells and their contribution to the column density

The "collect-and-collapse" scenario proposes that the ionising flux of OB-type stars indeed efficiently sweeps up the gas located within the H II region extent and develops a shell at the periphery of H II bubbles (Elmegreen & Lada 1977).

We (see also Appendix E) investigate the contribution of this very narrow component to the column density measured with *Herschel*. This contribution should be especially large at the border of the H II regions where the line of sight tangentially crosses the shell.

We thus chose to model the density structure of a shell surrounding an H II region, similar to the one powered by the Mon R2-IRS1 star. We used a density structure that linearly increases with the radius, $\rho(r) \propto r$ (see Fig. 3) to mimic those suggested by the calculations of H II region expansion
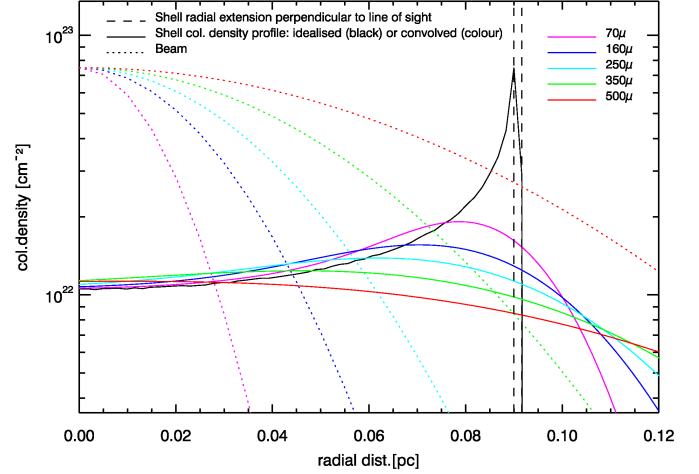

Fig. D.1. Contribution of the shell to the column density profile of the central UCH II region. Its density radial extension is given by the two dashed black lines. The column density resulting from the line-of-sight accumulation is illustrated by the black solid line. The shell column density is then convolved with the *Herschel* beams (coloured dotted lines) to simulate the flux or column density of the shell (coloured solid lines) observable from 6″ (70 μm) to 36″ (500 μm) resolutions.

(Hosokawa & Inutsuka 2005, 2006), giving more weight to the shell outer layers, and a thickness of ∼0.002 pc as modelled by Pilleri et al. (2013, Fig. 2). Pilleri et al. (2012, 2013) studied the shell of the central Mon R2 UCH II and considered two concentric slabs with homogeneous density, located at ∼0.08 pc around the H II region. In their model, the photo-dissociation region slab has a density of 2×10^5 cm^{-3} and a 6.5×10^{-4} pc thickness, while the high-density shell has a 3×10^6 cm^{-3} density and a 10^{-3} pc thickness. We used the densities of these slabs to model the inner and outer density values of the shell surrounding the central UCH II region.

Figure D.1 shows the column density result of the central UCH II shell calculated with the assumptions above, the idealised profile of this shell (black solid line), flat towards the centre and sharply increasing to the border. The shell was convolved with the *Herschel* beams (dotted coloured lines) to evaluate its contribution to the fluxes and column density profiles measured towards this H II region. The border increase due to the shell seen tangentially is completely smeared out for all *Herschel* wavelengths tracing the cold gas density, i.e. for $\lambda \geq 160\,\mu$m (see Fig. D.1). The column density profiles measured by *Herschel* have angular resolutions that are too coarse (25″ and 36″), by factors of at least four. On top of that, the mixing along the line of sight with other density components, such as the envelope and background filaments, means that the centre-to-limb contrast of the shell is rarely observable. We thus cannot expect to resolve any shell around compact or ultracompact H II regions located at 830 pc. In contrast in the case of the extended northern H II region, the relative contribution of the shell compared to the envelope is more important, increasing the centre-to-limb contrast and allowing a marginal detection of the shell (see Fig. 8). Therefore, the shell is not a dominant component of the column density structure of H II regions and their surroundings, but it cannot always be neglected for its complete bubbling.

Appendix E: Column density dilution on the central line of sight by shell

E.1. Attenuation by shell in homogenous envelope

We first assumed the simple scenario of a bubble expanding in an homogenous envelope where which all the matter initially located within a sphere with a $R_{\mathrm{H\,II}}$ radius concentrates in the shell located at this very same radius. According to numerical simulations, the H II region's swept-up shells have small thicknesses, $L_{\mathrm{shell}} < 0.01$ pc (e.g. Hosokawa & Inutsuka 2005). The almost total mass transfer from the bubble to the shell thus leads to the approximate equation,

$$M_{\mathrm{initial}} = \frac{4}{3}\pi R_{\mathrm{H\,II}}{}^{3} \times \rho_{\mathrm{initial}}$$

$$= M_{\mathrm{shell}} \simeq 4\pi R_{\mathrm{H\,II}}{}^{2} L_{\mathrm{shell}} \times \rho_{\mathrm{shell}}, \tag{E.1}$$

where ρ_{initial} is the initial constant density of the envelope, and ρ_{shell} the shell density, assumed to be homogeneous. Using the relation between ρ_{shell} and ρ_{initial} given by Eq. (E.1), the column density of the shell, Σ_{shell}, measured along the line of sight towards the centre of the region simply relates to that of the initial gas sphere, $\Sigma_{\mathrm{initial}}(r < R_{\mathrm{H\,II}})$, with homogeneous density ρ_{initial} and radius $R_{\mathrm{H\,II}}$ through

$$\Sigma_{\mathrm{shell}} = \Sigma_{\mathrm{obs}} = 2 \times (L_{\mathrm{shell}} \times \rho_{\mathrm{shell}})$$

$$\simeq 2 \times (R_{\mathrm{H\,II}} \times \rho_{\mathrm{initial}}/3) = \Sigma_{\mathrm{initial}}/3. \tag{E.2}$$

The column density measured towards the center of H II regions with fully developed bubbles is thus expected to be divided by three compared to its original value:

$$\eta_{\mathrm{shell}} = \frac{\Sigma_{\mathrm{initial}}}{\Sigma_{\mathrm{obs}}} = 3. \tag{E.3}$$

When approaching the border of the H II region, the line of sight crosses a greater part of the shell, and the column density reaches higher values. However, as shown in Appendix. D, the very small size expected for the shell will result in a beam dilution with very small enhancement that is usually not observable.

In the case of an H II region of radius $R_{\mathrm{H\,II}}$ that not fully developed within an envelope of density ρ_{initial}, to reach its external radius, R_{env}, the contribution of the outer residual envelope, Σ_{env}, needs to be accounted for. The initial column density is now $\Sigma_{\mathrm{initial}}(r < R_{\mathrm{env}}) = 2 \times R_{\mathrm{env}} \times \rho_{\mathrm{initial}}$. The column density observed towards the developed H II bubble would thus be

$$\Sigma_{\mathrm{obs}} = \Sigma_{\mathrm{shell}} + \Sigma_{\mathrm{env}} \simeq \Sigma_{\mathrm{initial}}/3 \times \frac{R_{\mathrm{H\,II}}}{R_{\mathrm{env}}} + \Sigma_{\mathrm{initial}} \times \frac{R_{\mathrm{env}} - R_{\mathrm{H\,II}}}{R_{\mathrm{env}}}$$

$$\simeq \Sigma_{\mathrm{initial}} \times \frac{3 \times R_{\mathrm{env}} - 2 \times R_{\mathrm{H\,II}}}{3 \times R_{\mathrm{env}}}, \tag{E.4}$$

and the decreasing factor or line-of-sight attenuation factor, η, would be

$$\eta = \frac{\Sigma_{\mathrm{initial}}}{\Sigma_{\mathrm{obs}}} \simeq \frac{3}{3 - 2 \times \frac{R_{\mathrm{H\,II}}}{R_{\mathrm{env}}}}. \tag{E.5}$$

It can be noticed that for a fully extended H II region that reaches the size of the envelope $R_{\mathrm{H\,II}} = R_{\mathrm{env}}$, the attenuation factor reaches 3, the value already obtained for the shell alone.

These purely geometrical attenuation factors are weak for the small compact and ultra-compact H II regions ($\eta \simeq 1.1/1.2$), but

start to be noticeable for the more extended northern H II region ($\eta \simeq 1.5$). We could estimated the density of the initial protostellar envelope before the H II region develops, ρ_{initial}, by correcting the mean density $\langle\rho_{\mathrm{obs}}\rangle$, measured in Sect. 3.4.1 from observed column density through Eq. (3). The density correction due to the geometrical effect of H II region expansion is obtained by the following relation: $\rho_{\mathrm{initial}} \sim \langle\rho_{\mathrm{obs}}\rangle \times \eta$.

E.2. Attenuation in an envelope of decreasing density

In the more realistic case of an envelope with a decreasing density gradient, it is expected that the attenuation factor of the column density by H II bubbles, η, should be greater than in the case of a constant-density envelope and constantly increasing as the H II region expands.

The mass collected in the shell for the expansion of the H II region at a radius $R_{\mathrm{H\,II}}$ is given by Eq. (A.2). The density in the shell of thichness L_{shell} is, then,

$$\rho_{\mathrm{shell}} = \frac{M(R_{\mathrm{H\,II}})}{4\pi R_{\mathrm{H\,II}}^{2} L_{\mathrm{shell}}} = \frac{\rho_{1} R_{\mathrm{H\,II}}^{1-q}}{(3-q) \times L_{\mathrm{shell}}}.$$

The column density observed for this shell at small impact parameter, near the H II region centre is then

$$\Sigma_{\mathrm{shell}}(R_{\mathrm{H\,II}}) = \rho_{\mathrm{shell}} \times L_{\mathrm{shell}} = \rho_{1} \frac{R_{\mathrm{H\,II}}^{1-q}}{3-q}.$$

The initial value of the column density was

$$\Sigma_{\mathrm{initial}}(R_{\mathrm{H\,II}}) = \int_{0}^{R_{\mathrm{H\,II}}} \rho(r)\,\mathrm{d}r = \int_{0}^{R_{\mathrm{H\,II}}} \rho_{1} r^{-q}\,\mathrm{d}r = \rho_{1} \frac{R_{\mathrm{H\,II}}^{1-q}}{1-q}. \tag{E.6}$$

This relation is valid only for $q < 1$ when the value of R^{1-q} near 0 is negligible. The attenuation by the shell is given by

$$\eta_{\mathrm{shell}} = \frac{\Sigma_{\mathrm{initial}}}{\Sigma_{\mathrm{obs}}} = \frac{3-q}{1-q}. \tag{E.7}$$

For constant density envelope ($q = 0$), Eq. (E.3) is recovered.

To evaluate the attenuation with an existing residual outer envelope we have to calculate the corresponding column density contribution,

$$\Sigma_{\mathrm{env}}(R_{\mathrm{H\,II}}) = \int_{R_{\mathrm{H\,II}}}^{R_{\mathrm{env}}} \rho(r)\,\mathrm{d}r = \frac{\rho_{1}}{1-q} R_{\mathrm{env}}^{1-q}\left(1 - \left(\frac{R_{\mathrm{H\,II}}}{R_{\mathrm{env}}}\right)^{1-q}\right), \tag{E.8}$$

then

$$\eta = \frac{\Sigma_{\mathrm{initial}}(R_{\mathrm{env}})}{\Sigma_{\mathrm{obs}}} = \frac{\Sigma_{\mathrm{initial}}(R_{\mathrm{env}})}{\Sigma_{\mathrm{shell}}(R_{\mathrm{H\,II}}) + \Sigma_{\mathrm{env}}(R_{\mathrm{H\,II}})}$$

will give, after some calculations,

$$\eta = \frac{3-q}{3 - 2 \times \left(\frac{R_{\mathrm{H\,II}}}{R_{\mathrm{env}}}\right)^{1-q} - q}. \tag{E.9}$$

For a shell reaching the size of the envelope $R_{\mathrm{H\,II}} = R_{\mathrm{env}}$, Eq. (E.9) leads to Eq. (E.7), which is obtained for the shell alone, and for a constant density envelope ($q = 0$) it gives Eq. (E.5)

These relations are only valid for $q < 1$, owing to the singularity at the origin of the density distribution.

E.3. Attenuation in envelope of decreasing density with a constant density core

To avoid the singularity at the origin we need to use the density profile defined by Eq. (A.5) with a central core of constant density ρ_c and a size of r_c. Following the same calculation as above they give for the mass

$$
\begin{aligned}
M(R) &= \int_0^R \rho(r) V(r) \, dr \\
&= \int_0^{r_c} \rho(r) V(r) \, dr + \int_{r_c}^R \rho(r) V(r) \, dr \\
&= \frac{4\pi\rho_1 R^{3-q}}{3-q} \left(1 - \frac{q}{3} \left(\frac{r_c}{R} \right)^{3-q} \right),
\end{aligned}
\tag{E.10}
$$

the density in the shell

$$
\rho_{\text{shell}} = \frac{M(R_{\text{H II}})}{4\pi R_{\text{H II}}^2 L_{\text{shell}}},
$$

the shell column density near the centre of the H II region

$$
\begin{aligned}
\Sigma_{\text{shell}}(R_{\text{H II}}) &= \rho_{\text{shell}} \times L_{\text{shell}} = \frac{M(R_{\text{H II}})}{4\pi R_{\text{H II}}^2} \\
&= \frac{\rho_1 R^{1-q}}{3-q} \left(1 - \frac{q}{3} \left(\frac{r_c}{R_{\text{H II}}} \right)^{3-q} \right),
\end{aligned}
\tag{E.11}
$$

the initial value of the column density

$$
\Sigma_{\text{initial}}(R_{\text{H II}}) = \frac{\rho_1 R_{\text{H II}}^{1-q}}{1-q} \left(1 - q \left(\frac{r_c}{R_{\text{H II}}} \right)^{1-q} \right),
\tag{E.12}
$$

and then the attenuation by the shell

$$
\eta_{\text{shell}} = \frac{\Sigma_{\text{initial}}}{\Sigma_{\text{obs}}} = \frac{3-q}{1-q} \times \frac{1 - q(r_c/R_{\text{H II}})^{1-q}}{1 - \frac{q}{3}(r_c/R_{\text{H II}})^{3-q}}.
\tag{E.13}
$$

All these relations reduces to the equivalent one of the previous section for $r_c = 0$.

The same calculations as before for an existing residual outer envelope are still applicable here. As shown by Franco et al. (1990), the shell develops only for $q < 1.5$, so $q < 3$, and the terms $\left(\frac{r_c}{R_{\text{H II}}} \right)^{3-q}$ in the equations above are always negligible. Then the calculations give

$$
\eta = \frac{3-q}{3 - 2 \times \left(\frac{R_{\text{H II}}}{R_{\text{env}}} \right)^{1-q} - q} \times \left(1 - q \left(\frac{r_c}{R_{\text{H II}}} \right)^{1-q} \right)
\tag{E.14}
$$

for the attenuation, and for $r_c = 0$ we recover Eq. (E.9)

The application to the northern H II region with appropriate values of the different parameters gives an attenuation factor $\eta \simeq 25$, which becomes ~ 100 when the H II region expansion reaches the size of the envelope ($R_{\text{H II}} = R_{\text{env}}$).

The formal treatment of the case of the compact and UCH II regions would require considering an envelope with two density gradients, but the attenuation would be as efficient as for the northern extended H II region once expansion of these region occurred.
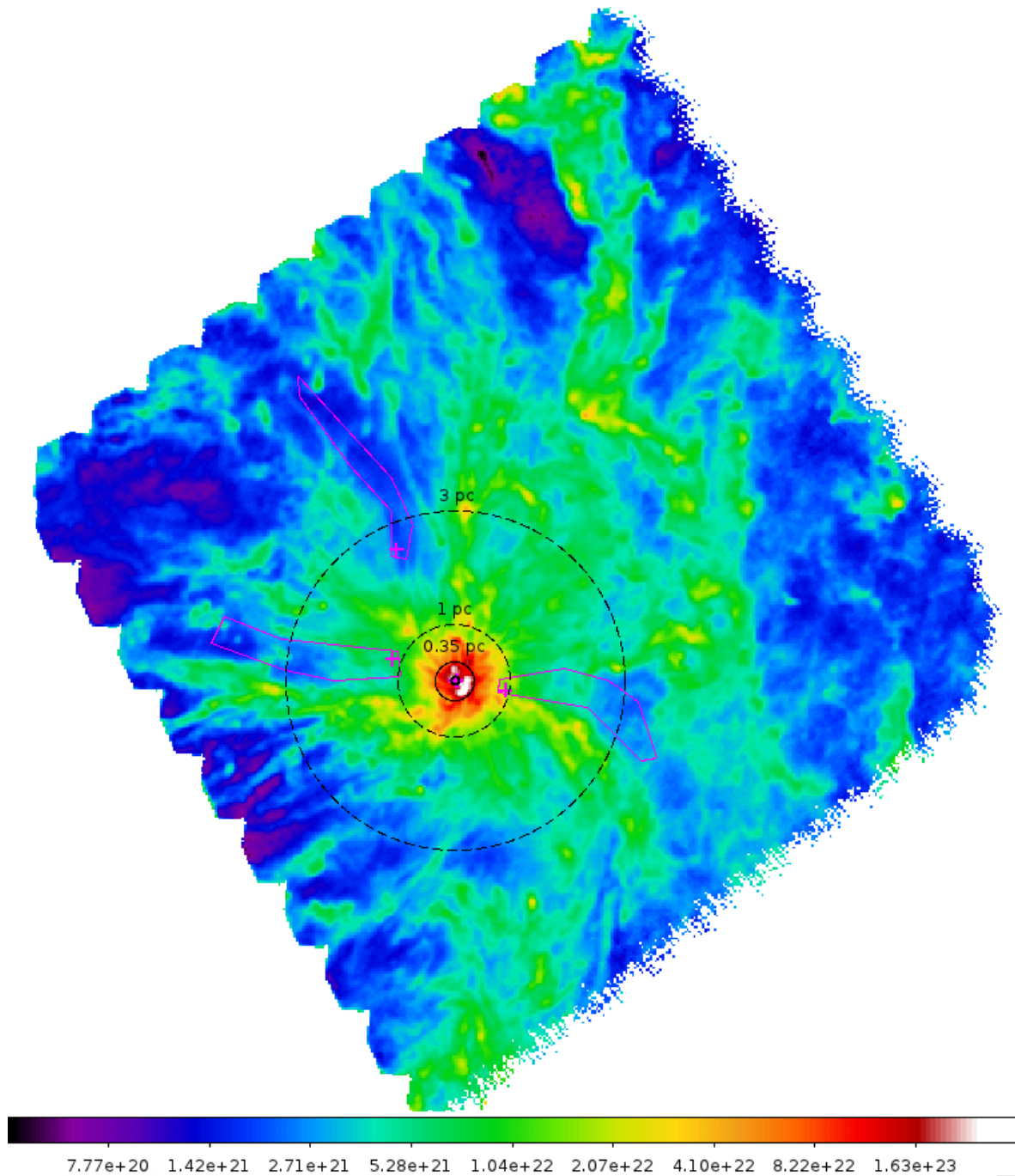
Appendix F: Additional figures

Fig. F.1. Column density map showing the azimuthal selection of areas used to characterise the density profiles of the eastern, western, and northern H II region envelopes. The H II region bubble, the inner, and the outer envelopes of the central UCH II region are outlined with dashed circles, whose sizes are given in Tables 1−3.
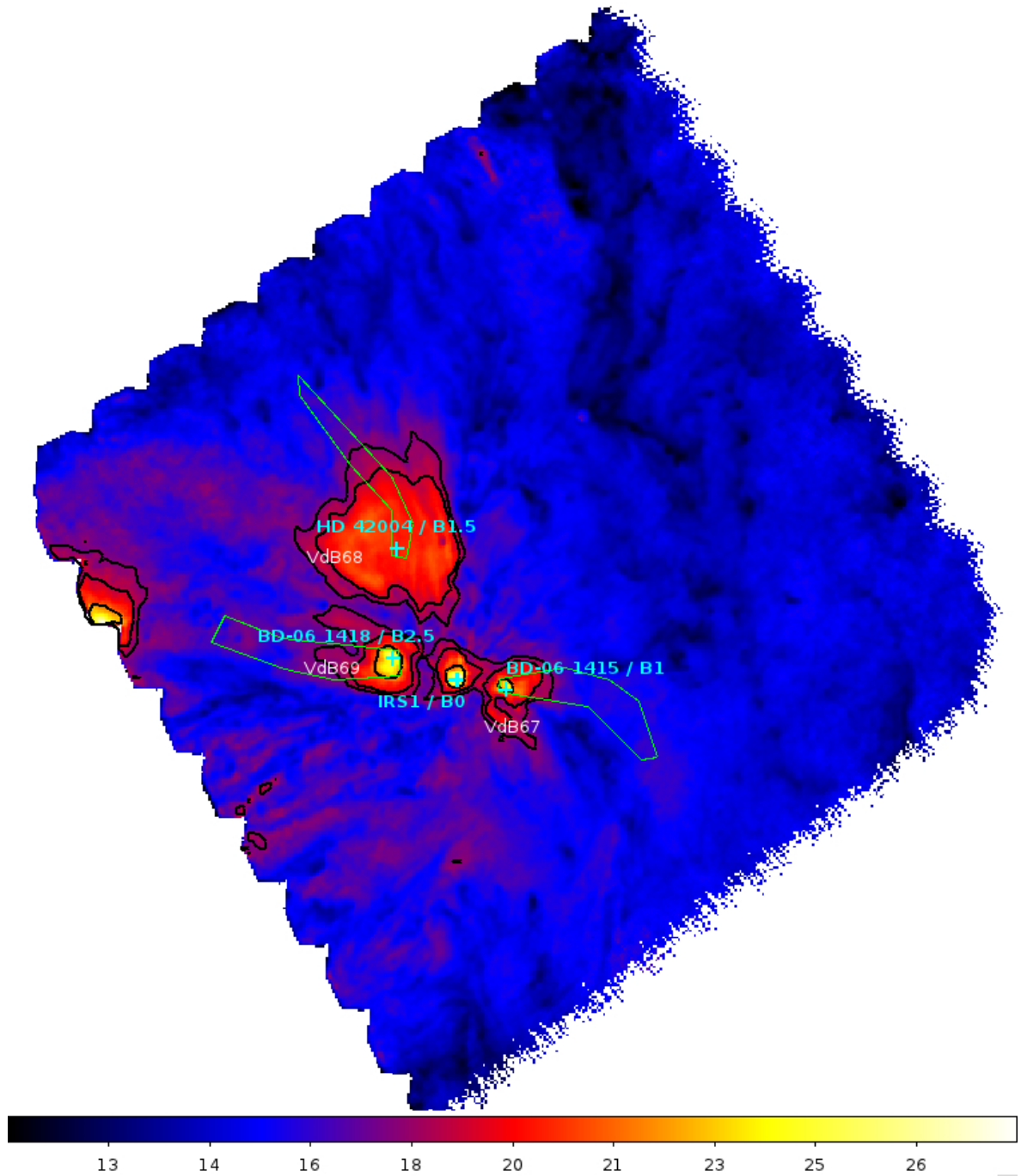
Fig. F.2. Hot regions overall contours of profile extraction on temp. map. Spectral type are taken from Racine (1968).